Author Manuscript

Author Manuscript

Author Manuscript

Author Manuscript

HHS Public Access

Author manuscript

Cell Rep. Author manuscript; available in PMC 2024 January 30.

Published in final edited form as:

Cell Rep. 2023 December 26; 42(12): 113466. doi:10.1016/j.celrep.2023.113466.

NGLY1 mutations cause protein aggregation in human neurons

Andreea Manole[1], **Thomas Wong**[1,10], **Amanda Rhee**[1,10], **Sammy Novak**[2], **Shao-Ming Chin**[1], **Katya Tsimring**[1], **Andres Paucar**[1], **April Williams**[3], **Traci Fang Newmeyer**[1], **Simon T. Schafer**[1], **Idan Rosh**[4], **Susmita Kaushik**[5,6], **Rene Hoffman**[7], **Songjie Chen**[7], **Guangwen Wang**[7], **Michael Snyder**[7], **Ana Maria Cuervo**[5,6], **Leo Andrade**[2], **Uri Manor**[2], **Kevin Lee**[8], **Jeffrey R. Jones**[1], **Shani Stern**[4], **Maria C. Marchetto**[9], **Fred H. Gage**[1,11,*]

[1]Laboratory of Genetics, The Salk Institute for Biological Studies, 10010 North Torrey Pines Road, La Jolla, CA 92037, USA

[2]Waitt Advanced Biophotonics Core, Salk Institute for Biological Studies, La Jolla, CA 92037, USA

[3]The Razavi Newman Integrative Genomics and Bioinformatics Core Facility, Salk Institute for Biological Studies, La Jolla, CA 92037, USA

[4]Sagol Department of Neurobiology, Faculty of Natural Sciences, University of Haifa, Haifa, Israel

[5]Department of Developmental and Molecular Biology, Albert Einstein College of Medicine, Bronx, NY 10461, USA

[6]Institute for Aging Studies, Albert Einstein College of Medicine, Bronx, NY 10461, USA

[7]Department of Genetics, Stanford University School of Medicine, Stanford, CA 94305, USA

[8]Grace Science Foundation, Menlo Park, CA 94025, USA

[9]Department of Anthropology, University of California, San Diego, La Jolla, CA 92093, USA

[10]These authors contributed equally

[11]Lead contact

SUMMARY

Biallelic mutations in the gene that encodes the enzyme N-glycanase 1 (NGLY1) cause a rare disease with multi-symptomatic features including developmental delay, intellectual disability,

This is an open access article under the CC BY-NC-ND license (http://creativecommons.org/licenses/by-nc-nd/4.0/).

*Correspondence: gage@salk.edu.

AUTHOR CONTRIBUTIONS

A.M., F.H.G., M.C.M., and K.L. conceived the project. A.M. and F.H.G. designed experiments and wrote the manuscript with contributions from all authors. A.M., A.R., T.W., and K.T. performed experiments and collected data. S.N., L.A., and U.M. performed TEM, SEM, and correlative light and electron microscopy (CLEM) experiments. S.T.S. and I.R. performed the electrophysiology experiments and analysis. T.F.N., S.-M.C., S.K., and A.M.C. performed analysis and interpretation of mass spectrometry. G.W., R.H., S.C., and M.S. provided the iPSCs and collected data. A.M. and A.W. carried out RNA-seq and proteomic analysis. A.P. generated astrocytes from the NGLY1 cohort and performed analysis. A.M., A.R., and T.W. carried out image analyses. A.M. analyzed and interpreted data. M.C.M. and F.H.G. supervised the project.

DECLARATION OF INTERESTS

The authors declare no competing interests.

SUPPLEMENTAL INFORMATION

Supplemental information can be found online at https://doi.org/10.1016/j.celrep.2023.113466.

Author Manuscript Author Manuscript Author Manuscript Author Manuscript

neuropathy, and seizures. NGLY1's activity in human neural cells is currently not well understood. To understand how NGLY1 gene loss leads to the specific phenotypes of NGLY1 deficiency, we employed direct conversion of NGLY1 patient-derived induced pluripotent stem cells (iPSCs) to functional cortical neurons. Transcriptomic, proteomic, and functional studies of iPSC-derived neurons lacking NGLY1 function revealed several major cellular processes that were altered, including protein aggregate-clearing functionality, mitochondrial homeostasis, and synaptic dysfunctions. These phenotypes were rescued by introduction of a functional NGLY1 gene and were observed in iPSC-derived mature neurons but not astrocytes. Finally, laser capture microscopy followed by mass spectrometry provided detailed characterization of the composition of protein aggregates specific to NGLY1-deficient neurons. Future studies will harness this knowledge for therapeutic development.

In brief

Manole et al. employ cutting-edge techniques including laser capture microscopy to scrutinize the protein aggregates accumulating in NGLY1-deficient neurons. Their study unveils a significant enrichment of specific proteins associated with neurodegenerative diseases, providing novel insights into the pathological mechanisms underlying NGLY1 deficiency and shedding light on potential therapeutic targets.

Graphical Abstract

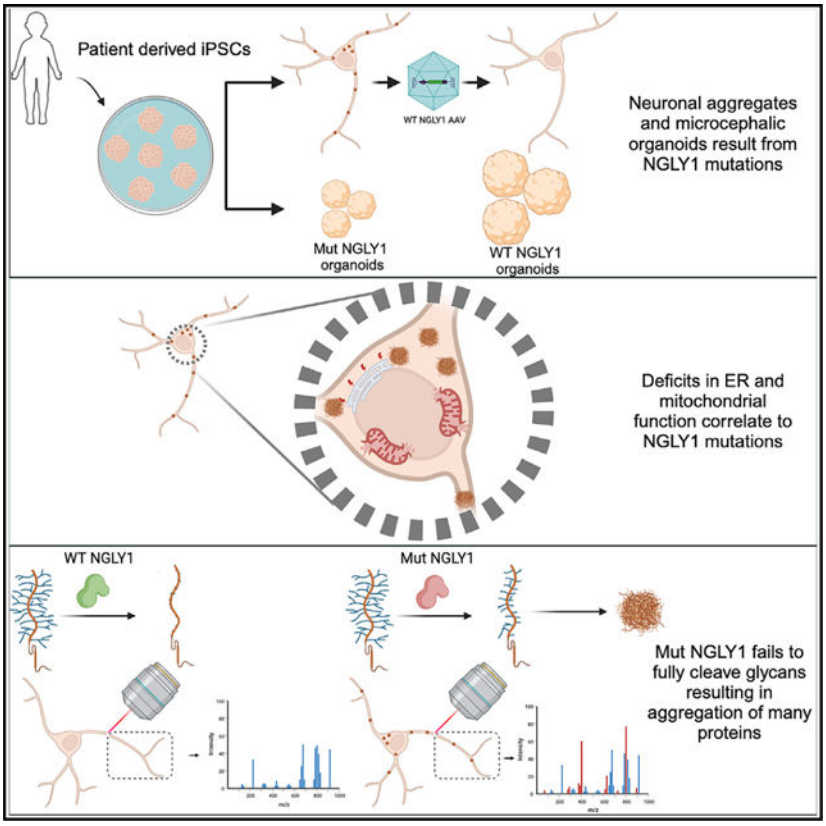

Author Manuscript Author Manuscript Author Manuscript Author Manuscript

INTRODUCTION

The cytosolic N-glycanase 1 (Ngly1) is an evolutionarily conserved de-glycosylating enzyme that plays a critical role in the quality control of newly synthesized glycoproteins by removing N-glycans from asparagine (Asn) residues of misfolded glycoproteins.[1,2] Loss-of-function mutations in the NGLY1 gene result in a severe systemic disorder called NGLY1 deficiency (MIM: 615273, 610661). Symptoms of NGLY1 deficiency include neuropathy with movement disorder, global developmental delay, acquired microcephaly, liver damage, chronic constipation, and the absence of tears.[3] Around half of affected individuals will develop clinical seizures.[4] Exact mechanisms by which NGLY1 loss leads to these specific phenotypes remains unknown, and no disease-modifying treatments are available. It is hypothesized that in the absence of NGLY1 function, defects in the endoplasmic-reticulum-associated protein degradation (ERAD) pathway, proteasome activity, autophagy, and mitochondrial quality control lead to damage in cells of the brain, liver, and peripheral tissues, but biochemical evidence of such damage and human cell models to support these ideas are lacking.[3,5,6]

Loss-of-function mutations in png-1, the *Caenorhabditis elegans* ortholog of NGLY1, lead to aberrant neuronal branching, possibly related to the peripheral neuropathy seen in patients.[7] Recently described NGLY1 knockout rodent models show neuro-behavioral defects, movement disorders, and somatosensory impairment reminiscent of the phenotypes of human NGLY1 deficiency patients.[8] Loss of NGLY1 in these rodent models also leads to accumulation of cytoplasmic ubiquitinated proteins, necrotic lesions, mineralization, intra- and extracellular eosinophilic bodies, astrogliosis, microgliosis, and significant loss of mature neurons in several parts of the nervous system.[8,9] Other mutants of NGLY1 and its orthologs have been analyzed in various organisms to elucidate the molecular function, pathways, and substrates of NGLY1.[10–17] NGLY1's deglycosylation activity appears essential for the activation of the transcription factor NFE2L1, which regulates expression of proteasome subunits.[6,14] NGLY1 has also been reported to act through NFE2L1 to influence mitochondrial function[18] and inflammation.[15] In a *Drosophila* model, NGLY1's deglycosylation activity has been shown to modulate tissue-specific bone morphogenetic protein (BMP) signaling.[19] NGLY1 is reported to regulate expression of multiple aquaporins across species, and its absence disrupts the Atf1/Creb1 signaling pathway in mouse embryonic fibroblasts.[20] These findings show that NGLY1 has various roles in cellular signaling, which could explain the vastrange of symptoms that individuals with NGLY1 deficiency experience.

However, the role of NGLY1 activity in human neural cells is currently not well understood, and there is a need to develop human neural cell models to study the consequence of NGLY1 loss and to evaluate potential therapeutic approaches to treat or slow disease progression. Human induced pluripotent stem cells (iPSCs) provide an attractive alternative to traditional models for the study of genetic diseases with a neurological component, as they can differentiate into the cells present in the neural niche, allowing for the early stages of neuronal development to be examined *in vitro* along with the functional properties of mature neurons in culture. Additionally, these cells can be readily isolated for downstream phenotypical assays such as transcriptional, proteomic, and metabolomic

Author Manuscript Author Manuscript Author Manuscript Author Manuscript

profiles to identify pathways for clinical intervention. Furthermore, iPSC-derived neural cells provide a long-term resource for the screening of drugs that could potentially recover some of the deficiencies related to the disruption of pathway caused by NGLY1 mutation.

Here, we established an iPSC-derived neuronal model and reported novel phenotypes of neurons associated with NGLY1 deficiency. We present for the first time an underlying molecular mechanism of these defects that suggests possible therapeutic strategies for treating NGLY1-deficient patients. Investigations into NGLY1's role in the neurodegenerative phenotype of NGLY1 deficiency could help develop better approaches for clinical management of this devastating condition.

RESULTS

Transcriptomic and proteomic analysis of NGLY1 neurons

All iPSC lines used in this study were reprogrammed from fibroblasts from three patients carrying homozygous or compound heterozygous loss-of-function alleles of NGLY1[21] (Figure 1C) and displaying developmental delay, intellectual disability, a complex hyperkinetic movement disorder, or, in some cases, seizures.[3] Isogenic control lines were created by CRISPR-mediated genome editing to restore one or both deleterious alleles to the corresponding functional allele (Figure 1C).

We generated neurons from the iPSCs of NGLY1-deficient patients and control lines, employing a rapid single-step induction of functional neurons using lentiviral overexpression of pro-neuronal gene Ngn2 (Figures 1A and 1B). This conversion strategy gives rise to a major fraction of functional glutamatergic neurons and a very minor fraction of GABAergic cells in a short period of time.[22]

To identify the genes and processes that drive phenotypes of NGLY1 deficiency, we performed RNA sequencing (RNA-seq) from 4-week-old NGLY1-deficient patient and control neurons. Unsupervised hierarchical clustering and principal-component analysis of NGLY1 and control neurons derived from iPSC lines revealed that patient and control neurons clustered separately (Figures 1D and S1A). NGLY1 gene transcript levels were reduced in the patient neurons (Figure S1B). Importantly, we repeated this experiment and found similar separation, indicating good reproducibility of neuronal conversion, sorting, and the RNA-seq pipeline. Moreover, differential expression analysis using DESeq-2 revealed over 3,000 genes that were highly significantly differentially expressed in NGLY1-deficient patients compared to controls. Interestingly, gene set analysis indicated that genes corresponding to ER stress, autophagy, proteasome processes, and ribonucleoproteins were mostly upregulated (Figures 1E, S1C, and S1D). Also, many genes relating to synaptic processes, oxidative stress response, and mitochondria-related processes were found to be differentially expressed. These data suggest that NGLY1-deficient patient neurons show defective protein aggregate-clearing functionality, mitochondrial defects, and synaptic dysfunctions.

With this knowledge, we next generated proteomics data from total protein extracts of NGLY1-deficient patient and control neurons after 4 weeks of differentiation. A total of

Author Manuscript Author Manuscript Author Manuscript Author Manuscript

339 proteins were identified to be differentially expressed between patient and control neurons, with 116 proteins being downregulated and 221 proteins being upregulated (Figure 1F). Upregulated proteins included those related to protein processing in ER processes, sphingolipid signaling, and Huntington's disease (Figure 1G). Interestingly, proteins related to oxidative stress response, cysteine/methionine metabolism, and N-glycan biosynthesis were found to be downregulated in NGLY1-deficient patients (Figure 1G).

Phenotypical characterization of NGLY1 neurons

We next characterized the functional changes in the neuronal cells derived from NGLY1-deficient patients. Neuronal morphology, including cell size, neurite outgrowth, and branching were examined. Immunocytochemistry assays were used to evaluate the size and complexity of the neuronal processes in neurons from NGLY1-deficient patients and controls. An increase in the number of bead-like swellings in neuronal processes in the NGLY1-deficient patients was observed compared to the controls (Figure 2A). Neuritic beading is an early hallmark of neuronal toxicity induced in a variety of pathological conditions, including mitochondrial disease.[23] Given the overlap of NGLY1-deficiency phenotypes with those of mitochondrial disorders such as developmental delay, neuropathy, muscle weakness, and seizures,[4] we examined the mitochondria of NGLY1-deficient neurons in more detail. MTCO2 (mitochondrial protein) immunostaining revealed that mitochondria in NGLY1-deficient neurons (Mut) were severely fragmented (Figures 2B and 2C), in contrast to the tubular mitochondrial structure observed in wild-type (WT) control cells. Next, we investigated mitochondrial function in patient and control neurons by measuring the mitochondrial membrane potential (MMP) using the JC-1 assay (Figure 2D). Flow cytometry analysis revealed that NGLY1-deficient neurons showed decreased red/ green ratios, indicative of impaired mitochondrial function (Figure 2E). These findings are consistent with our RNA-seq data presented above and with previous reports in other NGLY1-deficient cell types.[15,18,24,25]

Using whole-cell patch clamp, we then assessed functional features of Mut neurons. Cells were typically held in current-clamp mode near −60 mV with a steady holding current, and current injections of 12 pA current below the steady current that was needed to hold the cell at −60 mV in 3-pA steps for a 400-ms duration. A total of 35 depolarization steps were injected in current-clamp mode. Neurons with a holding current that was larger than 50 pA were discarded from the analysis. The excitability was assessed as the total evoked action potentials in these 35 depolarization steps. One patient-derived line (Mut1) was hypoexcitable compared to control, whereas two others (Mut2 and Mut3) were hyperexcitable (Figures 2F and 2G).

Excitatory postsynaptic currents (EPSCs) were recorded from control (WT) and patient-derived (Mut) neurons in voltage-clamp mode holding the cells at −70 mV. Significant differences were observed both in the rate and amplitude of EPSCs for the three mutant lines. The mean rate of EPSCs was 0.63 ± 0.19 Hz (standard error) in WT neurons, while in Mut1 neurons, it was 0.39 ± 0.2 Hz; it was even further reduced to 0.06 ± 0.026 Hz in Mut2 neurons and to 0.13 ± 0.018 Hz in Mut3 neurons. The mean amplitude of EPSCs was 38.4 ± 3.7 pA in control neurons but was significantly decreased to 27.5 ± 1.4 pA in Mut2 neurons

Author Manuscript Author Manuscript Author Manuscript Author Manuscript

and further decreased in Mut1 neurons to 17.4 ± 0.3 pA and in Mut3 neurons to 12.78 ± 1.58 pA (Figures 2H–2J). Overall, these experiments point to severe functional deficits of NGLY1-mutant neurons.

NGLY1 neurons develop ProteoStat-positive aggregates (PSPAs) that can be partially rescued

To investigate the presence of protein aggregates, we used a protein aggregation dye, ProteoStat (Enzo Life Science), a molecular rotor that is currently the only commercial dye marketed for protein aggregate detection for visible to subvisible aggregates in patient and control neurons. Super-resolution microscopy revealed that a large fraction of NGLY1-deficient neurons stained positively with this dye in basal conditions at 4 weeks of differentiation (Figure 3A), whereas no staining was observed in NGLY1-deficient cells at an earlier time point of 2 weeks of the differentiation. Aggregate staining was also not observed in other immature (dividing) NGLY1-deficient cell types including iPSCs or the neural precursor cells (NPCs) (Figures S2A and S2B), suggesting that differentiation and/or neuronal cell specificity seems to be an important factor for this aggregate formation.

We then confirmed the presence of these aggregates using ultrastructural examination of neurons (including axons, dendrites, and synaptic domains), where round electron-dense structures were observed in the NGLY1-deficient neurons in the soma and also neurites (Figures 3B, S3A, and S3B). Transmission electron microscopy (TEM) images indicated that these dark structures were big enough to distend the membranes of the thin neurites. These structures were mostly localized between the membrane and cytoskeletal fibers (Figure 3B). Since their sizes were similar to aggregates formed by addition of the proteasome inhibitor MG-132 for 24 h (Figure S3C), we hypothesized that they corresponded to ProteoStat-positive structures. Correlative confocal and electron microscopy confirmed the electron-dense structures observed by TEM correspond to the protein aggregates stained by ProteoStat (Figure 3C). Membrane extraction experiments observed by scanning electron microscopy (SEM) on the NGLY1 neurons also revealed expanded neurites with structures resembling aggregates seen previously by TEM. These aggregates were often surrounded by or associated with cytoskeletal fibers, matching our TEM data showing aggregates lodged between cytoskeletal filaments and the plasma membrane (Figures 3B and S3D).

To confirm that the formation of protein aggregates results from the loss of NGLY1 function, we performed rescue experiments by introducing a functional NGLY1 gene back into the NGLY1-deficient neurons shortly after initiating differentiation (Figure 3D). Prior to this step, stable iPSC lines were generated by transducing with lentiviral vector carrying the doxycycline-inducible (TRE-tight advanced promoter) pro-neuronal gene Ngn2 without GFP but still selectable for puromycin resistance, and we utilized our established protocol to generate functional neurons (Figure 3D). After 3 to 4 days of differentiation, the neurons were transduced with another lentiviral vector expressing NGLY1 2a GFP under a CAG promoter. Approximately 90%–95% of the transduced neurons were GFP positive, and overexpression of NGLY1 protein was detectable by western blot at 4 weeks post-differentiation (Figure S4A). Staining with the protein aggregation dye revealed a significant

Author Manuscript Author Manuscript Author Manuscript Author Manuscript

decrease in the number of NGLY1-deficient cells with aggregates after transduction with the functional NGLY1 gene relative to untransduced NGLY1-deficient cells at 4 weeks post-differentiation (Figures 3E and 3F). In addition, MMP of NGLY1-deficient cells transduced with the functional NGLY1 gene as measured by the JC-1 assay showed a restoration of MMP levels approaching that of controls (Figure S4B).

NGLY1 phenotypes appear to be predominantly observed in neurons

To determine whether these phenotypes were neuron specific, we generated astrocytes from the same iPSCs from NGLY1-deficient patients and controls (Figure 4A). We used a recently developed method to efficiently derive glial progenitor cells (GPCs) from pluripotent stem cells, including iPSCs and embryonic stem cells (ESCs), such that they can be propagated, expanded, and frozen as intermediates.[26] After 4–6 weeks of differentiation from the GPCs, we detected high expression of key astrocytic markers such as S100β and CD44 in both control and patient-derived cell lines at levels comparable to primary astrocytes (Figure 4B). In our previous findings, lower MMP, abnormal morphology and distribution of mitochondria were observed in NGLY1 neurons. In contrast to NGLY1-deficient neurons, the NGLY1-deficient astrocytes did not show lower MMP, abnormal morphology, or abnormal mitochondria under basal conditions at 6 weeks post-differentiation (Figures 4C–4E). Similarly, imaging with the protein aggregate dye showed no increase in aggregates in NGLY1-deficient astrocytes relative to control astrocytes under basal conditions at 6 weeks post-differentiation (Figure 4F). These data suggest that the loss of NGLY1 in astrocytes, in contrast to neurons, does not result in measurable changes in cell morphology mitochondrial function or in the accumulation of protein aggregates.

NGLY1 organoids have increased cell death and microcephaly

While conventional iPSC-based monolayer models capture human cell-type-specific processes, we generated three-dimensional brain organoids to assess the consequences of NGLY1 loss on cellular and structural organization within a patterned neuroepithelium comprising multiple cell types.[27,28] Since NGLY1-deficient patients develop acquired microcephaly, we sought to investigate how NGLY1 impacts early stages of human brain development using a standardized forebrain organoid protocol[29] with minor modifications (Figure 5A) and with Matrigel embedding to promote continuous neuroepithelium formation.[28] To increase oxygen exchange, cultures were maintained under agitating conditions[28,29] (protocol outlined in Figure 5A). Both control and NGLY1 iPSC-derived organoids consistently increased in size over time while forming neuroepithelial loops. NGLY1-derived organoids were of similar size and showed similar expansion rates (Figure 5B). Immunocytochemical analysis revealed that, at day 40 ± 5, organoids consisted of stratified neuroepithelial loops (Figures 5C and S5A) expressing the neural progenitor marker SOX2 and other forebrain markers (Figures 5D and S5C).

We further assessed the architecture of the neuroepithelial loops by determining the length of the apical and basal membrane and the diameter of the loops in NGLY1-deficient patient and control organoids at day 40 ± 3. There was a significant reduction in all parameters in NGLY1 organoids compared to controls (Figures 5D–5F and S5B). This reduction

Author Manuscript Author Manuscript Author Manuscript Author Manuscript

in neuroepithelium loop formation and growth rate is consistent with NGLY1-deficient patients' brains showing developmental delay and acquired microcephaly.[3,4]

The reduced brain size of NGLY1-deficient patients as well as the changes we observed in our organoid model might arise from impairments in several developmental processes including changes in NPC division, differentiation, or cell death. We next investigated apoptotic cell death in neuroepithelial progenitors as a potential underlying mechanism of the reduced size of loops in NGLY1 organoids by quantifying cleaved (active) caspase-3 at day 40 ± 5. This analysis revealed that apoptotic cell death was frequent in NGLY1 organoids and that there was a significant increase in the number of apoptotic neuroepithelial progenitors when comparing patient with control organoids (Figures 5G and 5H).

Next, we looked for the presence of protein aggregates in our organoids. While we did not observe increased numbers of aggregates in NGLY1-deficient organoids before day 70, after 70 days, there was a significant increase in PSPA staining outside the neuroepithelial loops in NGLY1-deficient organoids relative to control organoids (Figures 5I, 5J, and S5D). This localization of PSPA staining to regions containing differentiated post-mitotic neurons outside neuroepithelial loops is consistent with our observations that NGLY1 loss leads to protein aggregate accumulation selectively in mature neurons and not in actively dividing precursor cells.

Functional and structural characterization of NGLY1 PSPAs

To investigate the composition of the protein aggregates that accumulate in NGLY1-deficient neurons, we used laser capture microscopy (LCM)[30] to manually select neurites from differentiated NGLY1-deficient neurons, cut them with the laser, removed unwanted material, and thus concentrated on the aggregates characterized by mass spectrometry (Figure 6A). We identified a significant number of proteins that were exclusively detected in NGLY1-deficient (Mut-only) neurites (Figure 6B). The few proteins that were uniquely detected in the control (WT) neurons and those that were found in both WT and NGLY1-deficient (Mut-and-WT) neurites were mainly axonal proteins. The unique or over-represented hits found in the NGLY1-deficient neurites included proteins with associations with Parkinson's and Alzheimer's diseases and with pathways associated with the ubiquitin proteasomal system (UPS) responsible for protein degradation, folding, and intracellular trafficking (e.g., heat shock cognate proteins [HSPs]) and ribosomal proteins (Figure 6C). To confirm and validate proteins identified by LCM proteomic analysis and to exclude possible contaminating proteins, we used the following criteria to select candidates for further validation: (1) proteins selectively identified in NGLY1 neurites based on multiple peptides, (2) those with commercially available antibodies to detect the protein of interest, and (3) those candidates implicated in processes that might be relevant to NGLY1 disease even though their relationship to NGLY1 is unknown. With these criteria, we selected several proteins and performed immunofluorescence and western blotting experiments to validate the mass spectrometry findings. We found clear co-localization of several HSPA (Hsp70) family proteins and J-proteins in NGLY1-deficient neurites (Figures 6D, S6A, and S6B). In addition, total protein extracts revealed elevated expression of these proteins in NGLY1-deficient neurites (Figures 6E–6G and S6C).

Author Manuscript Author Manuscript Author Manuscript Author Manuscript

We next asked whether these proteins selectively identified in NGLY1-deficient neurites had intrinsic properties that would make them more prone to aggregation. Aggregation propensity is strongly dependent on amino acid composition; sequence, secondary, tertiary, and/or quaternary structure; and thermodynamic and kinetic stabilities and concentrations. Some of these properties are intrinsic, whereas others depend on the cellular environment. For this step, we used computational approaches to characterize the proteins selectively detected in the NGLY1-deficient neurites (Mut only) with those detected in both control and NGLY1-deficient neurites (Mut and WT proteins). We analyzed several parameters, including molecular weight, α-helical structures (no/weak correlation with aggregation), hydrophobicity, disulfide bridges (some correlation), turns, net charge (pI) (very high correlation), and β-sheet structures (high correlation in amyloid structures). The Mut-only proteins had a higher pI, higher turn count, and lower cysteine residues count (Figures 7A–7C), highlighting their higher propensity for aggregation. There was no difference in the other properties (Figures S7A–S7C). We next examined the relative amino acid content of the proteins enriched in our aggregates. Basic amino acids (Lys and Arg) were strongly enriched in Mut only, whereas acidic amino acids (Glu, Asp) were underrepresented (Figure S7D), which accounts for their higher pI compared to the Mut-and-WT proteins (Figure 7C). In addition, Gln was underrepresented in Mut-only proteins, suggesting that the proteins in these aggregates were distinct from the well-known amyloid-forming proteins.[31] We next verified whether the Mut-only proteins were predicted to be N-glycosylated. From our mass spectrometry data, we were able to observe that there was a total higher number of N-glycosylated proteins (predicted) in the Mut-only group (Figure S7E). To confirm this, we used immunofluorescence of succinylated wheat germ agglutinin (succ-WGA), which only binds to glycoconjugates containing GlcNAc. There was a clear overlap of succ-WGA staining with the PSPA staining in the NGLY1-deficient neurites (Figure S7G). Moreover, total protein extracts revealed an overall increase in GlcNAc-linked proteins in the NGLY1-deficient neurons compared to WT (Figure S7F). We were therefore able to propose a model of aggregation based on our findings, which is outlined in Figure 7D.

DISCUSSION

Key mechanisms causing neurological symptoms in NGLY1 deficiency are unknown, and there is no treatment available. Since live neurons from patients are unavailable and post-mortem tissues are unobtainable, iPSC-based model systems offer an unparalleled method for modeling and investigating mechanisms of disease. The present work has revealed that absence of NGLY1 leads to several neuronal phenotypes in iPSC-derived cortical neurons from NGLY1-deficient patients, including defects in mitochondrial morphology and function and the presence of intracellular protein aggregates. Here, we provide a platform and establish functional assays that can enable validation of additional protein candidates and cellular processes and can lead to identification of potential targets for decreasing the presence of protein aggregates.

Our NGLY1 transcriptome data revealed changes in several processes that, when disturbed, can lead to protein aggregation. For instance, ER stress occurs when misfolded proteins accumulate in the ER lumen,[32] and disruption of proteasomal processes or autophagy contribute to pathology of a variety of diseases.[33–35] Our bulk proteomic data showed

Author Manuscript Author Manuscript Author Manuscript Author Manuscript

a downregulation in N-glycan biosynthesis in NGLY1 neurons that might result from compensatory changes due to an accumulation of GlcNAc in these cells.

In one study, biochemical analysis in muscle of NGLY1-deficient patients showed a strongly reduced ATP production rate, whereas individual OXPHOS enzyme activities varied from normal to reduced.[25] Mitochondrial morphofunction fibroblast analysis showed patient-specific differences. We also observed differences in MMP in NGLY1 neurons. Therefore, variants in NGLY1 affect mitochondrial energy metabolism, which in turn might contribute to the clinical disease course. Other studies have shown that NGLY1 function is required for the activity of the transcription factor NFE2L1, a regulator of proteasome and mitophagy genes. Loss of NGLY1 and altered processing of NFE2L1 results in severely fragmented mitochondrial network in patient and Ngly1 mutant mouse embryonic fibroblasts.[15] We also noted fragmentation of the mitochondrial network when assessing the mitochondrial morphology in patient iPSC-derived neurons. In the NGLY1 neurons, whole-cell patch clamp revealed lower rates and amplitudes of EPSCs, as well as hyperexcitablity in some patient cell lines, which may reflect the occurrence of seizures in some, but not all, patients.

NGLY1 is thought to be essential in ERAD processes, as it deglycosylates misfolded glycoproteins that are then degraded by the proteasome.[2,36] Aberrant processing and accumulation of N-linked glycoproteins and evidence of ERAD dysregulation were observed in NGLY1 knockout mouse embryonic fibroblast cells,[2] most notably under conditions of proteasome inhibition.[2,37] Some ubiquitin-positive inclusions have also been noted in neurons of *Ngly1*$^{-/-}$ rats[8] and mice.[9] In our work, we present detailed characterization of the protein aggregates resulting from iPSC-derived NGLY1-deficient neurons using super-resolution light microscopy and electron microscopy. There was no significant amyloid component, and, based on the imaging, these aggregates were likely amorphous in nature. The occurrence of this phenotype was reduced when we introduced the NGLY1 gene back into the neurons, providing evidence that the aggregates were specifically due to the absence of NGLY1 function. Notably, we did not detect similar protein aggregates in the corresponding NGLY1-deficient astrocytes derived from the same iPSCs, suggesting that aggregation may be cell-type specific or may depend on specific cellular conditions such as proteostatic stress.[2] It is known that while astrocytes rely on glycolysis as their primary energy source, neurons predominantly rely on mitochondrial oxidative phosphorylation. Astrocytes' high glycolytic capacity allows them to support neuronal energy demands and maintain CNS homeostasis. Neurons, with their specialized functions, require high energy levels provided by mitochondrial metabolism. These differences in energy metabolism between astrocytes and neurons can influence proteostasis and potentially contribute to variations in protein aggregate formation. We did, however, observe a similar phenotype in NGLY1 organoids at a later stage, suggesting that cell differentiation and maturation play important roles in aggregate formation. As with human NGLY1 deficiency, the NGLY1 organoids manifest a microcephaly phenotype that may result from increased cell death. Increased apoptosis was also noted in the acquired form of microcephaly resulting from Zika virus exposure.[38] Future studies should investigate the mechanism of microcephaly and examine a distinct role for the NGLY1 gene in cortical development and malformation.

Author Manuscript Author Manuscript Author Manuscript Author Manuscript

One way to better understand the pathogenesis of NGLY1 diseases is to examine the content of protein aggregates. In contrast to the targeted and hypothesis-driven approaches that have been used before, it has become increasingly clear that the discovery process can be greatly enhanced with proteomics, an unbiased and extensive analysis of proteins in any given cell, organelle, or body fluid.[39] In this study, we successfully used this technique together with LCM, a cutting-edge technology for isolating pure cell populations or parts of cells from a heterogeneous tissue sample,[40] to characterize the components of the aggregates that accumulated in NGLY1-deficient neurites. Our investigation represents the first extensive proteomic investigation of NGLY1 protein aggregates, and its results can lead to advances in other protein-related aggregated disorders. Amorphous aggregates result from the accumulation of large amounts of misfolded proteins during proteostasis imbalances such as protein unfolding stresses, deregulated protein synthesis, degradation, or conformationally destabilizing mutations and glycosylation status. Newly synthesized proteins tend to be especially vulnerable to misfolding events, and widespread protein aggregation is thought to be toxic, particularly when the proteostasis network is disrupted.[41] Interestingly, misfolded proteins are known to be detected by DNAJs and refolded into biologically active states by members of the Hsp70 family, which have been implicated in a wide variety of cellular processes, including protection of the proteome from stress, folding and transport of newly synthesized polypeptides, activation of proteolysis of misfolded proteins, and the formation and dissociation of protein complexes.[42–44] Furthermore, Hsp70 has been shown to co-precipitate with α-syn in the Lewy bodies and Lewy neurites in patients with Parkinson's disease and to exhibit chaperone activity to prevent α-syn fibril formation both *in vitro* and *in vivo.*[45,46] More recently, DNAJA2 levels have been found to be upregulated in affected neurons of patients with mild cognitive impairment and Alzheimer's disease.[47] Our LCM proteomic analysis of aggregates in NGLY1-deficient patient neurons reveals features shared with other aggregate-related disorders.

While this article was in revision, support for several of our findings was published. It has been demonstrated that the NGLY1 iPSC lines used in our study exhibit alterations in NGLY1 mRNA and protein levels.[48] Moreover, ERAD pathway gene alterations have been observed in patient-derived cell lines, which is consistent with the dysfunction of this pathway in NGLY1 deficiency. Additionally, GlcNAc-Asn accumulation, a characteristic feature of NGLY1 deficiency, has been observed in other NGLY1 knockout cell lines.[49]

Overall, our study contributes to the growing body of evidence on the pathological mechanisms of NGLY1 deficiency by utilizing iPSC-derived neuronal models. By characterizing the neuronal phenotypes and reviewing the relevant literature, we have established the validity of our NGLY1 iPSC model. These findings enhance our understanding of the disease and open avenues for further investigations into potential therapeutic targets. The comprehensive characterization of NGLY1 iPSC models is crucial for advancing the development of targeted therapies and improving clinical outcomes for patients with NGLY1 deficiency.

Future studies will develop more robust, highly predictive, and quantitative systems to explore the role of proteostasis networks in the regulation of aggregate formation

Author Manuscript Author Manuscript Author Manuscript Author Manuscript

and degradation in NGLY1 deficiency and will harness this knowledge for therapeutic development.

Limitations of the study

We acknowledge several limitations that should be taken into consideration when interpreting the findings. Firstly, it is important to note that our iPSC lines, which were used to model NGLY1 disease, have not been fully characterized in terms of meeting criteria for pluripotency and their capacity to differentiate into cells from all three germ layers.

Additionally, we employed ngn2 overexpression to derive one particular type of cortical neuron from iPSCs in other to model the NGLY1 disease. Other types of neurons are affected in NGLY1 deficiency, so further studies can investigate the presence of for example protein aggregates in different NGLY1-deficient neurons. Our LCM proteomic experiments capture only a single state of the aggregate composition (Figure 6). While we confirmed and validated several proteins identified by this method, research of the remaining hits can be the focus of ongoing studies. It would, moreover, be interesting to verify if any of these changes in elevated expression of the confirmed hits in NGLY1-deficient neurites can be reverted using genetic or drug therapies. Finally, further studies can investigate the contribution of ENGase on misfolded glycoproteins in NGLY1 deficiency and use this knowledge for therapeutic purposes.

STAR★METHODS

RESOURCE AVAILABILITY

Lead contact—Further information and requests for resources and reagents should be directed to and will be fulfilled by the lead contact, Fred H. Gage (gage@salk.edu).

Materials availability—This study did not generate new unique reagents.

Data and code availability

- RNA-seq counts from this study have been deposited to gene expression omnibus (GEO; GSE197454) and can be accessed using: https://www.ncbi.nlm.nih.gov/geo/query/acc.cgi?acc=GSE197454. The protein data can be found in the publicly accessible proteomics database, ProteomeXchange, using the https://doi.org/10.6019/PXD031091.
- This paper does not report original code.
- Any additional information required to reanalyze the data reported in this paper is available from the lead contact on request.

EXPERIMENTAL MODEL AND STUDY PARTICIPANT DETAIL

Cell lines—Patient cell lines used in this study were generously donated by Dr. Kevin Lee. Briefly, three NGLY1 patient and three control iPSC lines were used. Mut1 (4 year old caucasian female) is homozygous for two inherited mutations in NGLY1; Exon 11: pR452X and Exon 8: p.402_403del. This line is biologically related to WT1 (paternal) and WT2

Author Manuscript Author Manuscript Author Manuscript Author Manuscript

(maternal). Mut2 (4 year old male) contains homozygous p.R401* mutations. Mut3 (16 year old male) has mutations in exon 3: ps116x and intron 5: IVS5+5G>T. WT3 is a CRISPR corrected line derived from Mut1.

iPSC maintenance—This study protocol was approved by Salk Institute's IRB Committee (09–0003) and the Embryonic Stem Cell Research and Oversight Committee. The Salk Institute is committed to protecting the rights and welfare of human research participants and ensures compliance with all applicable ethical and legal requirements. IPSC colonies were plated onto Matrigel-coated plates (BD Biosciences) and maintained in mTeSR1 media (Stem Cell Technologies). All cell lines were regularly tested for mycoplasma contamination. Experiments were performed with one or two independent iPSC clones (for details see Figure 1C).

Direct conversion of human iPSCs into neurons—We transduced iPSCs with lentiviral particles for pLV-X-UbC:TetOn and pLV-X-Ngn2:2A:eGFP, and these were selected in the presence of puromycin (0.5 μg ml^{-1}, Sigma Aldrich) and G418 (100 μg ml^{-1}, Life technologies). For iPSC to induced neuron (iN) conversion, on day 0, iPSCs were treated with TrypLE Express (Gibco) and plated as dissociated cells on Matrigel-coated plates in PluriPro monolayer conditions (Cell Guidance Systems) with ROCK inhibitor Y27632 (10 μM, Stemcell Technologies). Medium was changed to PluriPro medium containing doxycycline (2 μg ml^{-1}, Stemcell Technologies). On day 3, iNs were treated again with TrypLE Express enzyme (Gibco) and plated on Matrigel coated plates in neuron maturation medium (containing N2 supplement (1×, Gibco), B27 supplement (1×, Gibco), laminin (2 μg/mL^{-1}, Invitrogen), BDNF (20 ng/ml, Peprotech), GDNF (20 ng/ml, Peprotech), cAMP (500ug/ml, TOCRIS) and doxycycline (2 μg ml^{-1}, Stemcell Technologies). On day 6, iNs were treated with TrypLE express and plated at desired concentrations in neuron maturation medium with added ROCK inhibitor (10 μM) onto plates coated with poly-ornithine (100 μg ml^{-1}, Sigma Aldrich) and laminin (100 μg ml^{-1}, Invitrogen). On day 7, medium was changed to neuron maturation medium without ROCK inhibitor. Following day 7, iNs underwent half medium changes with neuronal maturation medium for 3 weeks to obtain mature neurons. For RNA sequencing experiments, iNs were dislodged 4 days after conversion using TrypLE (Gibco), sorted based on eGFP expression and re-plated onto coverslips coated with poly-ornithine (100 μg ml^{-1}, Sigma Aldrich) and laminin (100 μg ml^{-1}, Invitrogen).

Cortical neuronal differentiation—iPSCs were differentiated into NPCs using the Livesey protocol with some modifications.[50] In brief, iPSCs were cultured in an adherent monolayer on Geltrex-coated plates. Neural induction was achieved using dual SMAD inhibition (1 μM dorsomorphin and 10 μM SB431542) in neural maintenance medium (DMEM/F-12, neurobasal, N-2, B-27, 5 μg/mL insulin, 1 mM L-glutamine, 100 μM non-essential amino acids, 100 μM 2-mercaptoethanol, 50 units/ml penicillin and 50 mg/mL streptomycin). After the formation of a neuroepithelial sheet, cells were passaged with Dispase II (Sigma) as small clusters onto wells coated with laminin. The subsequent differentiating cells were allowed to form neural rosettes in the presence of b-FGF and

Author Manuscript Author Manuscript Author Manuscript Author Manuscript

passaged until confluent and then frozen as cortical neural progenitor stocks around day 35. RT-qPCR and immunofluorescence microscopy confirmed the adoption of cortical identity.

Differentiation of astrocytes from iPSCs—iPSCs were cultured on matrigel-coated plates in mTeSR1 medium (STEMCELL Technologies) and differentiation into astrocytes was performed as described.[26] Embryoid bodies were generated from confluent iPSC cultures by mechanical dissociation with 1 mg/mL collagenase IV (Gibco) and then plated onto low-adherence plates in mTeSR1 medium containing 10 mM ROCK inhibitor (STEMCELL Technologies) and incubated overnight while shaking. The next day, the medium was changed to Astrocyte Medium (AM, ScienCell) with 500 ng/mL noggin (R&D Systems) and 10 ng/mL PDGFAA (PeproTech) for 14 days and was supplemented with only PDGFAA for an additional 7 days with agitation. Embryoid bodies were dissociated with papain (Papain dissociation system, Worthington), and the resulting GPCs were grown on 10 mg/mL poly-L-ornithine (poly-O, Sigma)- and 5 mg/mL laminin (Invitrogen)-coated plates in AM with 20 ng/mL FGF-2 (Joint Protein Central) and 20 ng/mL EGF (Humanzyme). Low-density GPC cultures were used for differentiation to astrocytes in DMEM/F-12 Glutamax, 2% B27 without vitamin A, 1% N2 (N2B27 media; all from Thermo Fisher Scientific) plus 10% SATO (Biowest). Cells were used 4–6 weeks post differentiation.

Generation of forebrain organoids—Forebrain organoids were generated as described previously with minor modifications.[29] On Day 0, human iPSC colonies were detached before reaching confluency with dispase and transferred to an Ultra-Low attachment 10 cm plate (Corning Costar) containing 10 mL TESR with ROCK inhibitor Y27632 (10 μM). hES medium consisted of DMEM:F12 (Invitrogen), 20% Knockout Serum Replacer (Lifetech), 1× Non-essential Amino Acids (Gibco), 1× 2-mercaptoethanol (Gibco), 1× GlutaMAX (Invitrogen), 10 ng ml^{-1} FGF-2 (Joint Protein Central) and ROCK inhibitor Y27632 (10 μM). 24 h later, on day 1, the medium was replaced with hES medium, consisting of DMEM:F12 (Invitrogen), 20% Knockout Serum Replacer (Lifetech), 1× Non-essential Amino Acids (Gibco), 1× 2-mercaptoethanol (Gibco), 1× GlutaMAX (Invitrogen), 10 ng ml^{-1} FGF-2 (Joint Protein Central), 2 μM LDN-193189 HCI (AdooQ) and 2 μM A83–01 (AdooQ). From day 2–4, detached colonies were fed with hES medium every day. On day 5, half the medium was replaced with neural induction medium consisting of DMEM:F12 (Invitrogen), 1× N2 Supplement (Invitrogen), 1× Non-essential Amino Acids (Invitrogen), 1× GlutaMAX (Invitrogen), 10 μg ml^{-1} Heparin (AdooQ), 1× Penicillin/Streptomycin (Sciencell), 10 μM CHIR99021 (AdooQ) and 1 μM SB-431542 (StemRD). On day 7, organoids were embedded in 25 μL Matrigel (Trevigen) droplets and continued to grow for an additional week in 6 cm Ultra-Low attachment plates (Corning Costar) in fresh neural induction medium. From day 14 onwards, organoids were transferred to an orbital shaker (80 rpm). On day 20, residual Matrigel was removed and medium was changed to differentiation medium comprising DMEM:F12 (Invitrogen), 1× N2 and B27 Supplements (Lifetech), 1× Non-essential Amino Acids (Gibco), 1× GlutaMAX (Invitrogen), 1× 2-Mercaptoethanol (Gibco), 1× Penicillin/Streptomycin (Sciencell) and 2.5 μg ml^{-1} Insulin (Sigma). Media changes were performed once a week using the aforementioned differentiation medium. On day 60, medium was changed to maturation medium comprising Neurobasal media, 1× B27 Supplements (Lifetech), 1× 2-mercaptoethanol, 0.2 mM ascorbic

Author Manuscript Author Manuscript Author Manuscript Author Manuscript

acid (Stemcell Technologies), 20 ng/mL BDNF (Peprotech), 20 ng/mL GDNF (Peprotech), 1 ng/mL TGFB1 (Proteintech), and 0.5 mM cAMP (TOCRIS). Media changes continued once a week. Organoids were assessed at day 40 and day 100.

METHOD DETAILS

FACS-based purification and RNA isolation—iPSC-iNs were detached using accutase (Stemcell Technologies) and then washed and stained with fluorophore-coupled antibodies (see supplementary methods) for 45 min at 4°C in PBS. Cells were washed, suspended in PBS and filtered using a 40-μm cell strainer. BD InFlux Cytometer (Becton-Dickinson) was used for FACS-based purification of neuronal cell types. The desired cell populations were sorted directly into Trizol-LS (Life Technologies). RNA was isolated according to the manufacturer's instructions and subsequently digested with TURBO DNase to remove trace quantities of DNA (ambion, Life Technologies). Before RNA-seq library preparation, assessment of RNA integrity numbers was performed using Agilent TapeStation.

RNA-seq and data preprocessing—Libraries were prepared using the TruSeq Stranded mRNA Sample Prep Kit according to the manufacturer's instructions (Illumina). We performed 75 base pair (bp) single-end sequencing using the Illumina HiSeq 2500 platform.

Analysis of the RNA-seq data was carried out by The Razavi Newman Integrative Genomics and Bioinformatics Core Facility at the Salk Institute. In brief, raw sequencing data were de-multiplexed and converted into FASTQ files using CASAVA software (v1.8.2). Quality of read sequences was tested using FASTQC (software developed Andrews, 2010; available online at http://www.bioinformatics.babraham.ac.uk/projects/fastqc/). Reads that passed QC(define) were mapped to the human genome (hg19) using STAR aligner software (v2.5.3a; Dobin et al., 2013) using default parameters (allowing up to ten mismatches, and up to nine multi-mapping locations, per read). Raw gene expression levels were quantified across all exons using the top-expressed isoforms as proxy for gene expression using HOMER v4.10 (Heinz S, Mol Cell, 2010). Variance-stabilizing transformation and differential gene expression was then carried out using the DESeq2 (v22.2, R/Bioconductor; Love et al., 2014) and EdgeR (v 3.24.3)[51] packages. The p values were corrected for multiple hypotheses testing using Benjamini-Hochberg false discovery rate (FDR) correction (Benjamin and Hochberg, 1995). The FDR threshold for significance was set at ≤0.1 and a log2 fold-change ≥1. R/Bioconductor (v3.5.0) graphical packages (pheatmap v1.0.12, ggplot2 v3.2.0, gplots v3.0.1.1, RColorBrewer v1.1–2) were used to visualize data by hierarchical clustering and to generate heat maps, Venn diagrams and PCA plots.

Gene ontology analysis—Functional annotation was performed using WebGestaltR v0.3.1[52] against the gene ontology biological process database (http://geneontology.org/). For differentially expressed genes and co-expression modules, the background was set to the total list of genes expressed in our dataset. Where indicated, significance of over-representation was adjusted to control the false discovery rate by means of the Benjamini–Hochberg procedure. The statistical significance threshold for all gene ontology analyses was $p < 0.05$.

Author Manuscript Author Manuscript Author Manuscript Author Manuscript

Immunocytochemistry—Cells were washed in PBS, fixed with 4% paraformaldehyde (PFA) for 30 min at room temperature and treated with PBS containing 0.1% Triton X-100 for 10 min. Cells were then blocked in PBS plus 5% BSA for 30 min at room temperature. Primary antibodies were incubated overnight at 4°C, washed three times with PBS, incubated with secondary antibodies for 1 h at room temperature, stained with DAPI solution and mounted in PVA-DABCO mounting solution (Sigma Aldrich). For confocal imaging, cells were grown on ibidi μ-slides. Antibodies and respective concentrations are listed in Supplementary Methods. The Proteostat Aggresome Detection Kit (Enzo) was used according to the manufacturer's instructions.

Forebrain organoids were fixed in 4% PFA for 2 h, washed with PBS, and incubated in 30% sucrose solution in an Eppendorf tube for 2–3 days at 4°C. Samples were embedded in TFM tissue freezing medium (General Data Healthcare), snap-frozen on dry ice and stored at −80°C. Cryostat was cleaned using 70% EtOH and samples were mounted and sectioned on chucks around −20°C. Sample blocks were trimmed at 50 μM until the samples were exposed. Twenty-μM sections were then obtained using the cryostat and mounted onto slides. Cut slides were stored at −80°C until stained.

For staining, hydrophobic barriers were drawn around the organoid sections, and the slides were washed with PBS 0.1% Triton X- for 10 min each. Samples were blocked for 30 min in blocking solution consisting of 5% horse serum and 0.3% Triton X-. Samples were then incubated with primary antibodies in blocking solution at room temperature for 1 h, washed with PBS, and then incubated with secondary antibodies and DAPI in blocking solution at room temperature for 1 h in the dark. Samples were washed with PBS, then mounted on coverslips using Immu-Mount solution, and stored at 4°C until imaging. Fluorescent signals were detected with the 63x on a Zeiss LSM 880 Rear Port Laser Scanning Confocal and Airyscan FAST Microscope.

Immunoblotting—iPSC-iNs were washed off with cold PBS and spun down for pellets. Whole-cell extracts were obtained by lysing the cells in ice-cold RIPA lysis buffer supplemented with protease and phosphatase inhibitor mixture, centrifuging at 14,000 RCF and 4°C for 10 min, and taking the supernatant. Protein concentration was determined via BCA assay. Protein samples were run on a 4–12% Bis-Tris Nu-PAGE gel and transferred to nitrocellulose membranes that were blocked in solution consisting of TBS, 0.1% Tween 20, and 5% BSA, and analyzed by immunoblotting. Antibodies and respective concentrations are listed in Supplementary Methods.

Mitochondrial function and morphology—Mitochondrial function and morphology were assessed using a combination of techniques. To evaluate mitochondrial membrane potential, we performed JC-1 staining followed by flow cytometry analysis. Briefly, cells were incubated with JC-1 dye for 30 min, and the red/green fluorescence ratio was measured using a flow cytometer. A decrease in the red/green ratio indicated a loss of mitochondrial membrane potential.

To assess mitochondrial morphology, cells were stained with MTCO2 antibody to label mitochondrial protein COX subunit II. After fixation, cells were permeabilized and blocked

Author Manuscript Author Manuscript Author Manuscript Author Manuscript

with a blocking buffer. Subsequently, cells were incubated with the primary antibody against MTCO2 overnight at 4°C, followed by incubation with a fluorescent secondary antibody for 1 h at room temperature. Nuclei were counterstained with DAPI. Fluorescent signals were detected with the 63x on a Zeiss LSM 880 Rear Port Laser Scanning Confocal and Airyscan FAST Microscope. z stack images were acquired at 0.2 μm intervals to capture the entire cellular volume. Mitochondrial morphology was classified into three categories based on the extent of fragmentation: tubular (long, interconnected mitochondria), more than 50% fragmented (mitochondria showing moderate fragmentation), and completely fragmented (highly fragmented and punctate mitochondria). Classification was performed manually by blinded observers, and at least 100 cells were analyzed per condition.

Quantification of mitochondrial morphology was expressed as the percentage of cells in each category.

Electrophysiology—Whole-cell patch clamp recordings were performed from eGFP highlighted neurons after 4 weeks of differentiation. The extracellular recording solution (128 mM NaCl, 5 mM KCl, 2 mM $CaCl_2$, 30 mM glucose, 1 mM $MgCl_2$ and 10 mM HEPES (pH 7.4)). The recording micropipettes (tip resistance 3–6 MΩ) were filled with internal solution (130 mM K-gluconate, 1 mM EGTA, 2 mM Mg-ATP, 0.3 mM Na-GTP, 5 mM Na-phosphocreatine and 10 mM HEPES (pH 7.4)). Recordings were made using Axopatch 700B amplifier (Axon Instruments). Signals were filtered at 6 kHz and sampled at 20 kHz. The series resistance was typically <15MΩ. For voltage-clamp recordings, the membrane potential was held at −70 mV. To record the sodium and potassium currents, cells were depolarized in 5-Mv increments. For current-clamp recordings, a hyperpolarized current was injected into the neuron to a membrane potential of −55 mV or −45 mV, depending on the experiments. Step-depolarized currents with identical parameters were injected into control and NGLY1-mutant neurons to elicit action potentials (APs). All recordings were performed at room temperature.

Electron microscopy (EM)—IPSC derived neurons were cultured on coverslips as above in for approximately 28 days. Materials were obtained from Electron Microscopy Sciences unless otherwise noted. Culture media was gently poured off and replaced with a fixative solution (2% paraformaldehyde and 2.5% glutaraldehyde in 0.1 M sodium cacodylate buffer with 2 mM calcium chloride at pH 7.4) pre-warmed to 37°C for 3 min at room temperature which was replaced with fresh ice-cold fixative and left overnight in the dark at 4°C. Fixative was poured out and exchanged with washes of ice-cold buffer (0.1 M sodium cacodylate buffer with 2 mM calcium chloride). Samples were post-fixed with 2% osmium tetroxide reduced with 1.5% potassium ferrocyanide in 0.1 M sodium cacodylate buffer with 2 mM calcium chloride at room temperature in the dark for 40 min, gently washed five times with distilled water and stained with 1% aqueous uranyl acetate overnight at 4°C. The following day, cells were dehydrated in a graded series of ice-cold ethanol until absolute, infiltrated with Eponate 12 resin, and polymerized at 60°C for 2 days. Coverslips were dissolved using concentrated hydrofluoric acid and small blocks were cut using a jewelers saw. Blocks were mounted on an Ultracut UC7 ultramicrotome (Leica) and 70-nm sections were cut with diamond knife (Diatome) and collected onto both copper grids for

Author Manuscript Author Manuscript Author Manuscript Author Manuscript

transmission electron microscopy (TEM) and silicon chips for imaging in the scanning electron microscope (SEM). TEM imaging was performed on a Zeiss Libra 120 at 80kV equipped with a Gatan Ultrascan 4k CCD camera. SEM imaging was performed on a Zeiss Sigma VP in high-vacuum/high-current mode at 3kV (WD: 9mm; Gatan BSD) with Atlas5 (Fibics) control system.

Correlative light and electron microscopy (CLEM)—Cells were cultured onto a gridded coverslip (CellVis D35–14-1.5GI) as above and the Proteostat Aggresome Detection Kit (ADK) was used as recommended for confocal imaging. Fixation was achieved as above for EM methods. After buffer rinses, neurons were inspected by fluorescence microscopy. A region of interest (ROI) was selected and Airyscan imaging was performed on a Zeiss 880 confocal microscope for ADK and eGFP/aldehyde autofluorescence signal. Following low- and high-resolution imaging of an appropriate field of view (minimum voxel size x, y, z: 0.036, 0.036, 0.297 μm), the coverslip was prepared for EM as above. SEM imaging of the ROI was performed as above with a minimum pixel size of 2nm. eGFP fluorescence and aldehyde autofluorescence provided unbiased fiducials for aligning the maximum projected view of the Airyscan data with the EM data, achieved using Bigwarp in ImageJ [https://ieeexplore.ieee.org/document/7493463].

Scanning electron microscopy (SEM)—Membrane extractions of live cells were prepared following.[53] After extraction, cells were fixed and prepared with alternated baths of aqueous 1% osmium tetroxide (EMS) and 1% tannic acid (Sigma–Aldrich), twice, for 1 h each and 3 washes of 10 min each in between. Samples were then dehydrated in a graded series of ethanol, critical-point dried (Baltec CPD 050), placed on carbon tape covering an aluminum holder, coated with 4 nm of platinum and observed in a FEG-SEM Zeiss Sigma VP, operated at 5 kV.

Laser capture microdissection—To prepare for laser capture microdissection (LCM), iPSC-iNs were plated onto membrane slides coated with poly-ornithine (100 μg ml^{-1}, Sigma Aldrich) and laminin (100 μg ml^{-1}, Invitrogen) in neuron maturation medium and cultured until matured. Following neuronal maturation, slides were taken for LCM. Maturation medium was carefully removed from the slides without detaching the neurons and LCM was immediately conducted. Neurites were identified at 40× magnification, marked using drawing tools, and laser capture was performed on these areas onto CapSure LCM macro caps. Laser energy was in the capture method (810 nm).

MS sample preparation and instrumentation—Samples were precipitated by methanol/chloroform and redissolved in 8 M urea/100 mM TEAB, pH 8.5. Proteins were reduced with 5 mM tris(2-carboxyethyl)phosphine hydrochloride (TCEP, Sigma-Aldrich) and alkylated with 10 mM chloroacetamide (Sigma-Aldrich). Proteins were digested overnight at 37°C in 2 M urea/100 mM TEAB, pH 8.5, with trypsin (Promega). Digestion was quenched with formic acid, 5% final concentration.

The digested samples were analyzed on a Fusion Lumos Orbitrap tribrid mass spectrometer (Thermo). The digest was injected directly onto a 30 cm, 75 μm ID column packed with BEH 1.7um C18 resin (Waters). Samples were separated at a flow rate of 300 nL/min on

Author Manuscript Author Manuscript Author Manuscript Author Manuscript

a nLC 1000 (Thermo). Buffer A and B were 0.1% formic acid in water and 0.1% formic acid in 90% acetonitrile, respectively. A gradient of 1–25% B over 100 min, an increase to 50% B over 20 min, an increase to 100% B over 10 min and held at 100%B for a final 10 min was used for 140 min total run time. Column was re-equilibrated with 15 μl of buffer A prior to the injection of sample. Peptides were eluted directly from the tip of the column and nanosprayed directly into the mass spectrometer by application of 2.5 kV voltage at the back of the column. The Orbitrap Fusion Lumos was operated in a data dependent mode. Full MS scans were collected in the Orbitrap at 120K resolution with a mass range of 400–1500 m/z and an AGC target of $4e^5$. The cycle time was set to 3 s, and within this 3 s the most abundant ions per scan were selected for CID MS/MS in the ion trap with an AGC target of $1e^4$ and minimum intensity of 5000. Maximum fill times were set to 50 ms and 100 ms for MS and MS/MS scans respectively. Quadrupole isolation at 1.6 m/z was used, monoisotopic precursor selection was enabled and dynamic exclusion was used with exclusion duration of 5 s.

Protein and peptide identification were done with Integrated Proteomics Pipeline – IP2 (Integrated Proteomics Applications). Tandem mass spectra were extracted from raw files using RawConverter[54] and searched with ProLuCID[55] against Uniprot human database. The search space included all fully-tryptic and half-tryptic peptide candidates. Carbamidomethylation on cysteine was considered as a static modification. Data was searched with 50 ppm precursor ion tolerance and 600 ppm fragment ion tolerance. Identified proteins were filtered to using DTASelect[56] and utilizing a target-decoy database search strategy to control the false discovery rate to 1% at the protein level.[57]

Mass spectrometry analysis—Protein ontology over-representation analysis of NGLY1 neurites was performed using WebGestaltR v 0.3.1 and the KEGG pathway database. Mass spectrometry data were mapped to the UniProt data to extract their protein annotation and overlaps between wild-type and mutant samples were calculated using R 3.5.0. Terms were considered over-represented using a false discovery threshold of 0.05.

QUANTIFICATION AND STATISTICAL ANALYSIS

Statistics were performed using GraphPad Prism 6. The significance between the variables was shown based on the p-value obtained (ns indicates $p > 0.05$, *$p < 0.05$, **$p < 0.005$, ***$p < 0.0005$). Data are presented as boxplots illustrating 80% of the data distribution, together with the median and 10th, 25th, 75th and 90th percentiles unless otherwise stated.

Supplementary Material

Refer to Web version on PubMed Central for supplementary material.

ACKNOWLEDGMENTS

We thank the patients and their families for providing tissue samples. This work was supported by the Grace Science Foundation. We thank Aamir Zuberi (Jackson Labs) and Matt Wilsey at the Grace Science Foundation for communications and coordination of reagent sharing. The authors thank L. Moore, A. Mendes, and K.E. Diffenderfer for technical assistance and M.L. Gage for editorial comments. We acknowledge the Salk Institute Stem Cell Core, Waitt Biophotonics Core, and Next Generation Sequencing Core for technical support. Funding to the cores was provided in part by NIH-NCI CCSG: P30 014195. This work was supported by the Mass

Author Manuscript Author Manuscript Author Manuscript Author Manuscript

Spectrometry Core of the Salk Institute with funding from NIH-NCI CCSG: P30 014195 and the Helmsley Center for Genomic Medicine. We thank J. Moresco, J. Diedrich, and A. Pinto for technical support. Other funding was provided by the JPB Foundation, the American Heart Association/Paul G. Allen Frontiers Group Brain Health & Cognitive Impairment Initiative (19PABHI34610000), the Dolby Charitable Trust, Leona M. and Harry B. Helmsley Charitable Trust #2017-PG-MED001, the Annette C. Merle-Smith and the G. Harold and Leila Y. Mathers Charitable Foundation, and NIH AG056306 to F.H.G. A.M. was funded by Alzheimer's Association Research Fellowship.

REFERENCES

1. Suzuki T, Huang C, and Fujihira H. (2016). The cytoplasmic peptide:N-glycanase (NGLY1) - Structure, expression and cellular functions. Gene 577, 1–7. [PubMed: 26611529]
2. Huang C, Harada Y, Hosomi A, Masahara-Negishi Y, Seino J, Fujihira H, Funakoshi Y, Suzuki T, Dohmae N, and Suzuki T. (2015). Endo-β-N-acetylglucosaminidase forms N-GlcNAc protein aggregates during ER-associated degradation in Ngly1-defective cells. Proc. Natl. Acad. Sci. USA 112, 1398–1403. [PubMed: 25605922]
3. Enns GM, Shashi V, Bainbridge M, Gambello MJ, Zahir FR, Bast T, Crimian R, Schoch K, Platt J, Cox R, et al. (2014). Mutations in NGLY1 cause an inherited disorder of the endoplasmic reticulum-associated degradation pathway. Genet. Med 16, 751–758. [PubMed: 24651605]
4. Lam C, Ferreira C, Krasnewich D, Toro C, Latham L, Zein WM, Lehky T, Brewer C, Baker EH, Thurm A, et al. (2017). Prospective phenotyping of NGLY1-CDDG, the first congenital disorder of deglycosylation. Genet. Med 19, 160–168. [PubMed: 27388694]
5. Freeze HH (2013). Understanding human glycosylation disorders: biochemistry leads the charge. J. Biol. Chem 288, 6936–6945. [PubMed: 23329837]
6. Tomlin FM, Gerling-Driessen UIM, Liu YC, Flynn RA, Vangala JR, Lentz CS, Clauder-Muenster S, Jakob P, Mueller WF, Ordoñez-Rueda D, et al. (2017). Inhibition of NGLY1 Inactivates the Transcription Factor Nrf1 and Potentiates Proteasome Inhibitor Cytotoxicity. ACS Cent. Sci 3, 1143–1155. [PubMed: 29202016]
7. Habibi-Babadi N, Su A, de Carvalho CE, and Colavita A. (2010). The N-glycanase png-1 acts to limit axon branching during organ formation in Caenorhabditis elegans. J. Neurosci 30, 1766–1776. [PubMed: 20130186]
8. Asahina M, Fujinawa R, Nakamura S, Yokoyama K, Tozawa R, and Suzuki T. (2020). Ngly1−/− rats develop neurodegenerative phenotypes and pathological abnormalities in their peripheral and central nervous systems. Hum. Mol. Genet 29, 1635–1647. [PubMed: 32259258]
9. Asahina M, Fujinawa R, Fujihira H, Masahara-Negishi Y, Andou T, Tozawa R, and Suzuki T. (2021). JF1/B6F1 Ngly1(−/−) mouse as an isogenic animal model of NGLY1 deficiency. Proc. Jpn. Acad. Ser. B Phys. Biol. Sci 97, 89–102.
10. Funakoshi Y, Negishi Y, Gergen JP, Seino J, Ishii K, Lennarz WJ, Matsuo I, Ito Y, Taniguchi N, and Suzuki T. (2010). Evidence for an essential deglycosylation-independent activity of PNGase in Drosophila melanogaster. PLoS One 5, e10545.
11. Seiler S, and Plamann M. (2003). The genetic basis of cellular morpho-genesis in the filamentous fungus Neurospora crassa. Mol. Biol. Cell 14, 4352–4364. [PubMed: 12960438]
12. Maerz S, Funakoshi Y, Negishi Y, Suzuki T, and Seiler S. (2010). The Neurospora peptide:N-glycanase ortholog PNG1 is essential for cell polarity despite its lack of enzymatic activity. J. Biol. Chem 285, 2326–2332. [PubMed: 19940117]
13. Gosain A, Lohia R, Shrivastava A, and Saran S. (2012). Identification and characterization of peptide: N-glycanase from Dictyostelium discoideum. BMC Biochem. 13, 9. [PubMed: 22682495]
14. Lehrbach NJ, and Ruvkun G. (2016). Proteasome dysfunction triggers activation of SKN-1A/Nrf1 by the aspartic protease DDI-1. Elife 5, e17721.
15. Yang K, Huang R, Fujihira H, Suzuki T, and Yan N. (2018). N-glycanase NGLY1 regulates mitochondrial homeostasis and inflammation through NRF1. J. Exp. Med 215, 2600–2616. [PubMed: 30135079]
16. Lehrbach NJ, Breen PC, and Ruvkun G. (2019). Protein Sequence Editing of SKN-1A/Nrf1 by Peptide:N-Glycanase Controls Proteasome Gene Expression. Cell 177, 737–750.e15. [PubMed: 31002798]

Author Manuscript Author Manuscript Author Manuscript Author Manuscript

17. Talsness DM, Owings KG, Coelho E, Mercenne G, Pleinis JM, Partha R, Hope KA, Zuberi AR, Clark NL, Lutz CM, et al. (2020). A Drosophila screen identifies NKCC1 as a modifier of NGLY1 deficiency. Elife 9, e57831.

18. Kong J, Peng M, Ostrovsky J, Kwon YJ, Oretsky O, McCormick EM, He M, Argon Y, and Falk MJ (2018). Mitochondrial function requires NGLY1. Mitochondrion 38, 6–16. [PubMed: 28750948]

19. Galeone A, Han SY, Huang C, Hosomi A, Suzuki T, and Jafar-Nejad H. (2017). Tissue-specific regulation of BMP signaling by Drosophila N-glycanase 1. Elife 6, e27612.

20. Tambe MA, Ng BG, and Freeze HH (2019). N-Glycanase 1 Transcriptionally Regulates Aquaporins Independent of Its Enzymatic Activity. Cell Rep. 29, 4620–4631.e4. [PubMed: 31875565]

21. Chen SA, Wang CY, Hsu CP, Lin JY, Cheng CT, Ouyang CH, Huang JF, and Liao CH (2021). Integration and comparison of multi-omics profiles of NGLY1 deficiency plasma and cellular models to identify clinically relevant molecular phenotypes. Preprint at bioRxiv.

22. Zhang Y, Pak C, Han Y, Ahlenius H, Zhang Z, Chanda S, Marro S, Patzke C, Acuna C, Covy J, et al. (2013). Rapid single-step induction of functional neurons from human pluripotent stem cells. Neuron 78, 785–798. [PubMed: 23764284]

23. Zheng X, Boyer L, Jin M, Kim Y, Fan W, Bardy C, Berggren T, Evans RM, Gage FH, and Hunter T. (2016). Alleviation of neuronal energy deficiency by mTOR inhibition as a treatment for mitochondria-related neurodegeneration. Elife 5, e13378.

24. Han SY, Pandey A, Moore T, Galeone A, Duraine L, Cowan TM, and Jafar-Nejad H. (2020). A conserved role for AMP-activated protein kinase in NGLY1 deficiency. PLoS Genet. 16, e1009258.

25. Panneman DM, Wortmann SB, Haaxma CA, van Hasselt PM, Wolf NI, Hendriks Y, Küsters B, van Emst-de Vries S, van de Westerlo E, Koopman WJH, et al. (2020). Variants in NGLY1 lead to intellectual disability, myoclonus epilepsy, sensorimotor axonal polyneuropathy and mitochondrial dysfunction. Clin. Genet 97, 556–566. [PubMed: 31957011]

26. Santos R, Vadodaria KC, Jaeger BN, Mei A, Lefcochilos-Fogelquist S, Mendes APD, Erikson G, Shokhirev M, Randolph-Moore L, Fred-lender C, et al. (2017). Differentiation of Inflammation-Responsive Astrocytes from Glial Progenitors Generated from Human Induced Pluripotent Stem Cells. Stem Cell Rep. 8, 1757–1769.

27. Eiraku M, Watanabe K, Matsuo-Takasaki M, Kawada M, Yonemura S, Matsumura M, Wataya T, Nishiyama A, Muguruma K, and Sasai Y. (2008). Self-organized formation of polarized cortical tissues from ESCs and its active manipulation by extrinsic signals. Cell Stem Cell 3, 519–532. [PubMed: 18983967]

28. Lancaster MA, Renner M, Martin CA, Wenzel D, Bicknell LS, Hurles ME, Homfray T, Penninger JM, Jackson AP, and Knoblich JA (2013). Cerebral organoids model human brain development and microcephaly. Nature 501, 373–379. [PubMed: 23995685]

29. Qian X, Nguyen HN, Song MM, Hadiono C, Ogden SC, Hammack C, Yao B, Hamersky GR, Jacob F, Zhong C, et al. (2016). Brain-Region-Specific Organoids Using Mini-bioreactors for Modeling ZIKV Exposure. Cell 165, 1238–1254. [PubMed: 27118425]

30. Bonner RF, Emmert-Buck M, Cole K, Pohida T, Chuaqui R, Goldstein S, and Liotta LA (1997). Laser capture microdissection: molecular analysis of tissue. Science 278, 1481–1483. [PubMed: 9411767]

31. Michelitsch MD, and Weissman JS (2000). A Census of Glutamine/asparagine-Rich Regions: Implications for Their Conserved Function and the Prediction of Novel Prions. Proc. Natl. Acad. Sci. USA 97. 11910–5. [PubMed: 11050225]

32. Bernales S, Papa FR, and Walter P. (2006). Intracellular signaling by the unfolded protein response. Annu. Rev. Cell Dev. Biol 22, 487–508. [PubMed: 16822172]

33. Bosco DA, LaVoie MJ, Petsko GA, and Ringe D. (2011). Proteostasis and movement disorders: Parkinson's disease and amyotrophic lateral sclerosis. Cold Spring Harb. Perspect. Biol 3, a007500.

34. Taylor RC, and Dillin A. (2011). Aging as an event of proteostasis collapse. Cold Spring Harb. Perspect. Biol 3, a004440.

Author Manuscript Author Manuscript Author Manuscript Author Manuscript

35. Schmidt M, and Finley D. (2014). Regulation of proteasome activity in health and disease. Biochim. Biophys. Acta 1843, 13–25. [PubMed: 23994620]
36. Suzuki T. (2015). The cytoplasmic peptide:N-glycanase (Ngly1)-basic science encounters a human genetic disorder. J. Biochem 157, 23–34. [PubMed: 25398991]
37. Maynard JC, Fujihira H, Dolgonos GE, Suzuki T, and Burlingame AL (2020). Cytosolic N-GlcNAc proteins are formed by the action of endo-β-N-acetylglucosaminidase. Biochem. Biophys. Res. Commun 530, 719–724. [PubMed: 32782141]
38. Ming GL, Tang H, and Song H. (2016). Advances in Zika Virus Research: Stem Cell Models, Challenges, and Opportunities. Cell Stem Cell 19, 690–702. [PubMed: 27912090]
39. Aebersold R, and Goodlett DR (2001). Mass spectrometry in proteomics. Chem. Rev 101, 269–295. [PubMed: 11712248]
40. Liu A. (2010). Laser capture microdissection in the tissue biorepository. J. Biomol. Tech 21, 120–125. [PubMed: 20808641]
41. Weids AJ, Ibstedt S, Tamás MJ, and Grant CM (2016). Distinct stress conditions result in aggregation of proteins with similar properties. Sci. Rep 6, 24554. [PubMed: 27086931]
42. Rampelt H, Kirstein-Miles J, Nillegoda NB, Chi K, Scholz SR, Morimoto RI, and Bukau B. (2012). Metazoan Hsp70 machines use Hsp110 to power protein disaggregation. EMBO J. 31, 4221–4235. [PubMed: 22990239]
43. Clerico EM, Tilitsky JM, Meng W, and Gierasch LM (2015). How hsp70 molecular machines interact with their substrates to mediate diverse physiological functions. J. Mol. Biol 427, 1575–1588. [PubMed: 25683596]
44. Nillegoda NB, Kirstein J, Szlachcic A, Berynskyy M, Stank A, Stengel F, Arnsburg K, Gao X, Scior A, Aebersold R, et al. (2015). Crucial HSP70 co-chaperone complex unlocks metazoan protein disaggregation. Nature 524, 247–251. [PubMed: 26245380]
45. Pemberton S, Madiona K, Pieri L, Kabani M, Bousset L, and Melki R. (2011). Hsc70 protein interaction with soluble and fibrillar α-synuclein. J. Biol. Chem 286, 34690–34699. [PubMed: 21832061]
46. Gao X, Carroni M, Nussbaum-Krammer C, Mogk A, Nillegoda NB, Szlachcic A, Guilbride DL, Saibil HR, Mayer MP, and Bukau B. (2015). Human Hsp70 disaggregase reverses Parkinson's-linked α-synuclein amyloid fibrils. Mol. Cell 59, 781–793. [PubMed: 26300264]
47. Mok SA, Condello C, Freilich R, Gillies A, Arhar T, Oroz J, Kadavath H, Julien O, Assimon VA, Rauch JN, et al. (2018). Mapping interactions with the chaperone network reveals factors that protect against tau aggregation. Nat. Struct. Mol. Biol 25, 384–393. [PubMed: 29728653]
48. Rauscher B, Mueller WF, Clauder-Münster S, Jakob P, Islam MS, Sun H, Ghidelli-Disse S, Boesche M, Bantscheff M, Pflaumer H, et al. (2022). Patient-derived gene and protein expression signatures of NGLY1 deficiency. J. Biochem 171, 187–199. [PubMed: 34878535]
49. Zhu L, Tan B, Dwight SS, Beahm B, Wilsey M, Crawford BE, Schweighardt B, Cook JW, Wechsler T, and Mueller WF (2022). AAV9-NGLY1 gene replacement therapy improves phenotypic and biomarker endpoints in a rat model of NGLY1 Deficiency. Mol. Ther. Methods Clin. Dev 27, 259–271. [PubMed: 36320418]
50. Shi Y, Kirwan P, and Livesey FJ (2012). Directed differentiation of human pluripotent stem cells to cerebral cortex neurons and neural networks. Nat. Protoc 7, 1836–1846. [PubMed: 22976355]
51. Robinson MD, McCarthy DJ, and Smyth GK (2010). edgeR: a Bio-conductor package for differential expression analysis of digital gene expression data. Bioinformatics 26, 139–140. [PubMed: 19910308]
52. Liao Y, Wang J, Jaehnig EJ, Shi Z, and Zhang B. (2019). WebGestalt 2019: gene set analysis toolkit with revamped UIs and APIs. Nucleic Acids Res. 47, W199–W205. [PubMed: 31114916]
53. Stern S, Debre E, Stritt C, Berger J, Posern G, and Knöll B. (2009). A nuclear actin function regulates neuronal motility by serum response factor-dependent gene transcription. J. Neurosci 29, 4512–4518. [PubMed: 19357276]
54. He L, Diedrich J, Chu Y-Y, and Yates JR (2015). Extracting Accurate Precursor Information for Tandem Mass Spectra by RawConverter. Anal. Chem 87, 11361–11367. [PubMed: 26499134]

Author Manuscript Author Manuscript Author Manuscript Author Manuscript

55. Xu T, Park SK, Venable JD, Wohlschlegel JA, Diedrich JK, Cociorva D, Lu B, Liao L, Hewel J, Han X, et al. (2015). ProLuCID: An improved SEQUEST-like algorithm with enhanced sensitivity and specificity. J. Proteomics 129, 16–24. [PubMed: 26171723]

56. Tabb DL, McDonald WH, and Yates JR (2002). DTASelect and Contrast: tools for assembling and comparing protein identifications from shotgun proteomics. J. Proteome Res 1, 21–26. [PubMed: 12643522]

57. Peng J, Elias JE, Thoreen CC, Licklider LJ, and Gygi SP (2003). Evaluation of multidimensional chromatography coupled with tandem mass spectrometry (LC/LC-MS/MS) for large-scale protein analysis: the yeast proteome. J. Proteome Res 2, 43–50. [PubMed: 12643542]

Author Manuscript Author Manuscript Author Manuscript Author Manuscript

Highlights

- NGLY1 neurons develop ProteoStat-positive aggregates that can be partially rescued
- Profiling protein aggregates unveils links to other neurodegenerative diseases
- NGLY1 phenotypes appear to be predominantly observed in neurons

Author Manuscript Author Manuscript Author Manuscript Author Manuscript

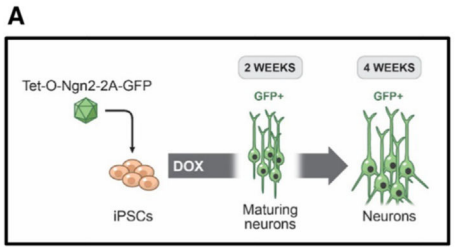

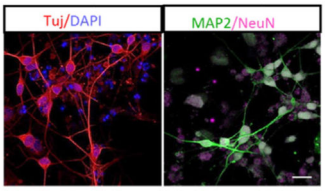

C

iPSC	Id in the paper	Maternal	Paternal
CP1	Mut1	Exon 8: p.402_403del	Exon 11: p.R542X
CP1-E8C	WT1	WT	Exon 11: p.R542X
CP1-E11C	WT2	Exon 8: p.402_403del	WT
CP1-E8-11C	WT3	WT	WT
CP2	Mut2	Exon 8: p.R401X	Exon 8: p.R401X
CP7	Mut3	Exon 3: p.S116X	Intron 5: IVS5+5G>T

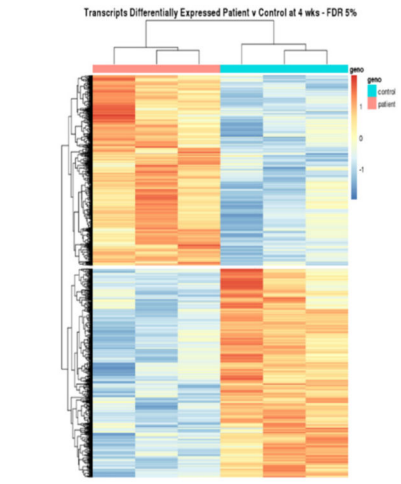

E

GO Term for Upregulated genes	Fold Enrichment	-log(FDR)
GO: 0010498: proteasomal protein catabolic process	2.86	4e-07
GO: 0006914: autophagy	2.93	7.1e-10
GO: 0072599: establishment of protein localization to ER	9.24	0
GO: 0070972: protein localization to ER	8.99	0
GO: 0071826: ribonucleoprotein complex subunit organization	3.76	6.1e-07
GO: 0070126: Mitochondrial translational termination	6.94	1.8e-08
GO: 0070125: mitochondrial translational elongation	6.23	1.3e-08
GO: 0045047: protein targeting to ER	9.8	0
GO: 0043161: proteasome-mediated ubiquitin-dependent protein catabolic process	2.54	1.1e-06
GO: 0042775: mitochondrial ATP synthesis coupled electron transport	5.46	6.5e-06
GO: 0042773: ATP synthesis coupled electron transport	5.23	7.7e-06
GO: 0042278: purine nucleoside metabolic process	2.12	2.4e-07
GO: 0042273: ribosomal large subunit biogenesis	6.6	9.9e-11
GO: 0042255: ribosome assembly	6.95	2.3e-10
GO: 0042254: ribosome biogenesis	4.25	0
GO: 0034976: response to ER stress	3.78	9.3e-07

GO Term for Downregulated genes	FE	-log(FDR)
GO: 1990138: neuron projection extension	3.54	3.2e-06
GO: 0098815: modulation of excitatory postsynaptic potential	5.59	9.9e-06
GO: 0061564: axon development	2.8	2.6e-06
GO: 0060996: dendritic spine development	4.82	4.2e-07
GO: 0060079: excitatory postsynaptic potential	4.94	3.6e-06
GO: 0060078: regulation of postsynaptic membrane potential	4.72	8.1e-08
GO: 0050804: modulation of synaptic transmission	3.85	3.5e-08
GO: 0050773: regulation of dendrite development	4.74	1.8e-08
GO: 0042391: regulation of membrane potential	3.99	1.9e-11
GO: 0034762: regulation of transmembrane transport	2.5	3.4e-07
GO: 0032535: regulation of cellular component size	2.94	6.8e-06
GO: 0031346: positive regulation of cell projection organization	4.05	6.4e-08
GO: 0007270: neuron-neuron synaptic transmission	4.59	3.8e-06
GO: 0007215: glutamate receptor signaling pathway	5.06	2.2e-08
GO: 0001508: action potential	4.96	1.4e-08
GO: 0000226: microtubule cytoskeleton organization	2.37	1.2e-06

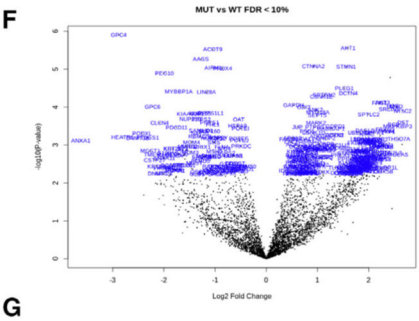

G

KEGG Term for Upregulated proteins	Fold Enrichment	-log(P.DE)
Huntington disease	23.8	0.0011
Arginine and proline metabolism	5.26	0.047
Sphingolipid signaling pathway	26.5	3.8e-07
Protein processing in ER	16.2	0.017
Fatty acid metabolism	9.26	0.042

KEGG Term for Downregulated proteins	Fold Enrichment	-log(P.DE)
Cysteine and methionine metabolism	4.8	7e-04
Biosynthesis of amino acids	5.36	0.027
Galactose metabolism	5.23	0.03
Metabolic pathways	19.23	0.0026
N-glycan biosynthesis	6.29	0.0087
Glutathione metabolism	4.55	0.013

Figure 1. Gene and protein network analysis of RNA and proteomic sequencing identifies several phenotypes associated with NGLY1 mutations

(A) Schematic of neuronal protocol showing subpopulations of GFP+ neurons over the time course of *in vitro* differentiation.

(B) Sample immunostaining images showing the expression of TuJ1/MAP2/NeuN in the NGLY1 neurons. Scale bar, 20 μm.

(C) Summary of NGLY1 variants.

(D) Unsupervised hierarchical clustering of top expressed genes from whole-transcriptome analysis (increased, red; decreased, blue) segregates NGLY1-deficient patients vs. controls and clusters patients and controls together.

(E) List of significantly enriched GO terms for uniquely upregulated genes (top) and downregulated genes (bottom). n = 3 independent experiments.

(F) Volcano plot illustrating differentially expressed proteins at 4 weeks post-differentiation. The –log10 (p value) is plotted against the log2 fold change of NGLY1-deficient patients vs. controls with significant threshold t test with false discovery rate (FDR) <0.001.

(G) List of significantly enriched KEGG terms for uniquely upregulated proteins (top) and downregulated proteins (bottom). n = 3 independent experiments.

Author Manuscript Author Manuscript Author Manuscript Author Manuscript

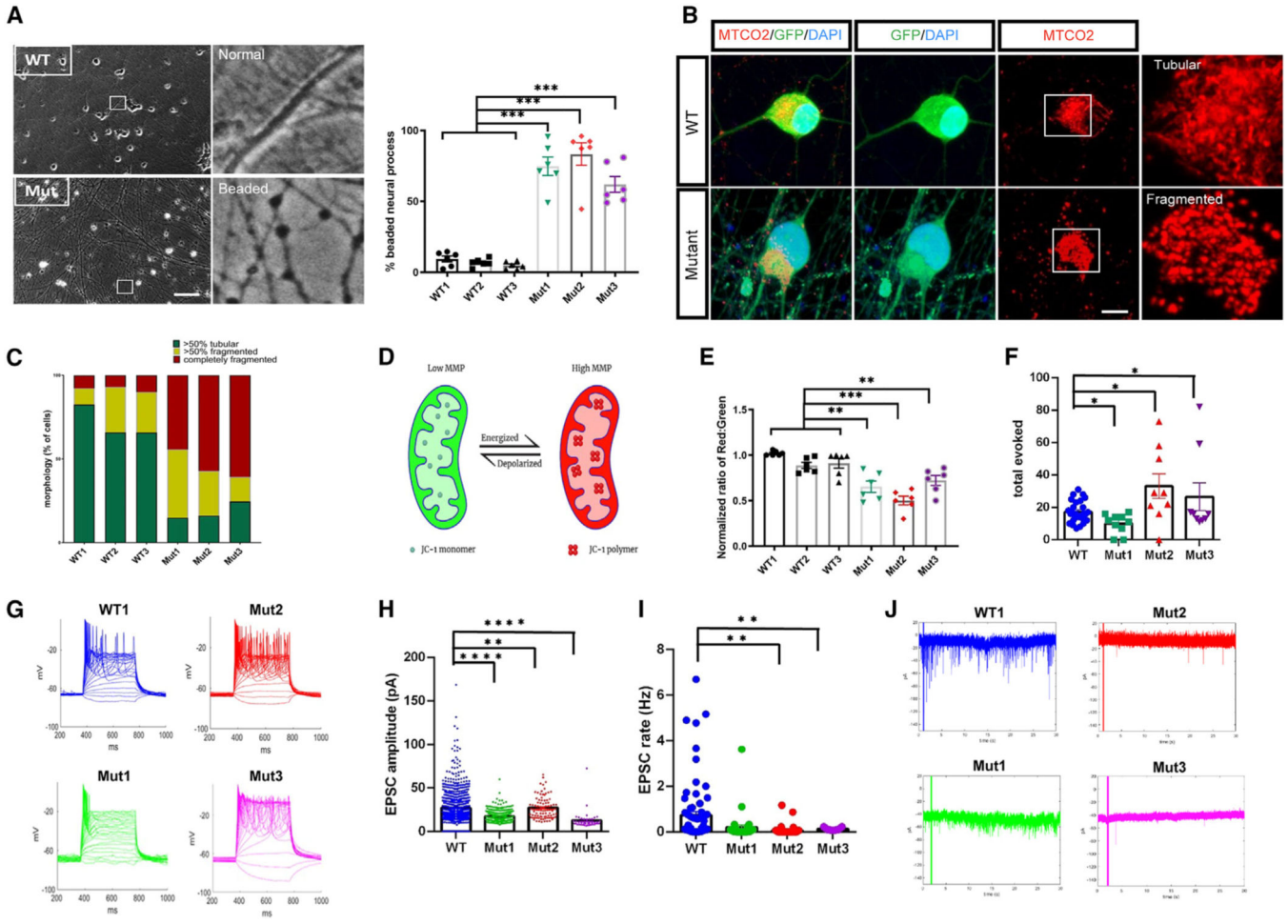

Figure 2. Neuronal phenotypes associated with NGLY1 mutations

(A) Representative phase-contrast image of control and NGLY1-deficient neurons at 4 weeks of differentiation. Scale bar, 30 μm. The percentage of neuronal processes containing neuritic beads was quantified by counting approximately 60 neuronal processes per line. Individual values are presented as a mean ± SEM. n = 3 experiments. ***$p < 0.0005$, one-way ANOVA with Dunnett's post hoc test.

(B) Representative immunofluorescence images of MTCO2 (mitochondrial marker) in WT1 and Mut2, with the proportion of mitochondria in each category is shown in (C), for all WT and NGLY1 mutant neurons at 4 weeks post-differentiation. Scale bar, 10 μm. ≥100 cells were enumerated for quantitation.

(D) Schematic rationale of JC-1.

(E) Quantification showing reduced MMP in NGLY1 neurons compared with controls. Individual measurements were performed in duplicate from 3 different experiments. **$p < 0.005$, ***$p < 0.0005$, one-way ANOVA with Dunnett's post hoc test.

(F) Abnormal excitability in 4-week-old neurons derived from NGLY1-deficient patients. The points represent the mean of each cell line (patient), n = 47 control neurons (all WT), n = 20 Mut1 neurons, n = 23 Mut2 neurons; n = 20 Mut3 neurons. *$p < 0.05$, t test.

Author Manuscript Author Manuscript Author Manuscript Author Manuscript

(G) Representative recordings in current-clamp mode of evoked potentials for a control (blue), Mut1 (green), Mut2 (red), and Mut3 (pink).

(H and I) Excitatory postsynaptic currents (EPSCs) recordings from 4-week-old NGLY1 neurons showing differences in amplitude and rate, respectively (as-terisks). n = 47 control neurons (all WT), n = 20 Mut1 neurons, n = 23 Mut2 neurons, n = 20 Mut3 neurons. **$p < 0.005$, ****$p < 0.00005$, t test.

(J) Representative EPSC traces for control (blue), Mut1 (green), Mut2 (red), and Mut3 (pink). WT1: CP1-E8C, WT2: CP1-E11C, WT3: CP1-E8–11C, Mut1: CP1, Mut2: CP2, and Mut3: CP7.

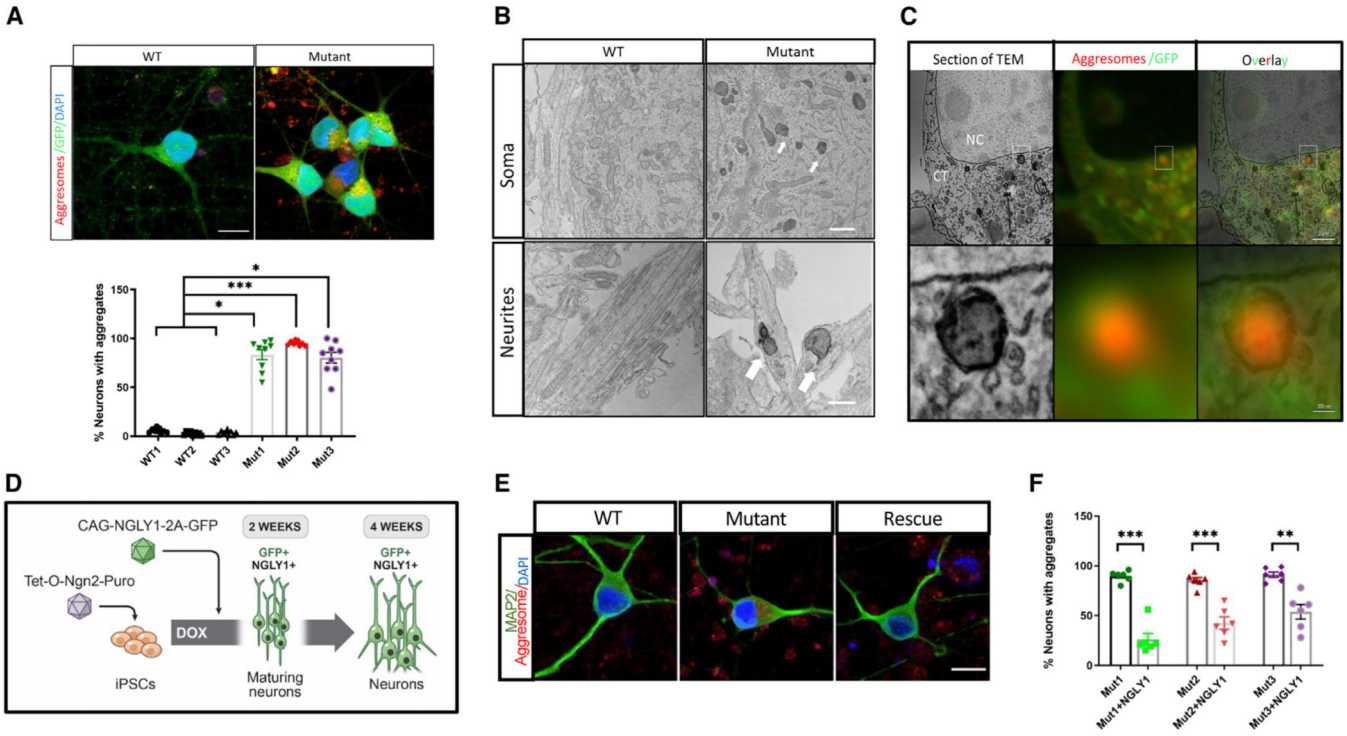

Figure 3. PSPA detection in NGLY1 neurons

(A) Representative images following staining with ProteoStat aggresome dye (red) on neurons derived from the iPSCs of NGLY1-deficient patients and isogenic control neurons. Neurons were stained 4 weeks after differentiation. GFP (green; NGN2 transduced neuron); DAPI (blue; nuclear stain). Yellow is due to overlap between GFP and the ProteoStat aggresome dye. The red staining in the background represents non-specific binding due to debris in the culture. Scale bar, 10 μm. The percentage of neurons positive for the Aggresome dye was quantified by counting approximately 120 neurons for WT and Mut. Individual values are presented as a mean ± SEM. *p < 0.05, ***p < 0.0005, one-way ANOVA with Dunnett's post hoc test.

(B) Representative electron micrographs showing cellular localization of electron-dense PSPAs (white arrows) in the soma (top) and neurites (bottom) of NGLY1 mutant neurons. Scale bars, (top) 1 μm and (bottom) 0.5 μm.

(C) Left: correlative light and electron microscopy showing that the fluorescent signal seen by confocal microscopy corresponds to intracellular electron-dense amorphous round structures in electron micrographs of the same region (CT, cytoplasm; NC, nucleus). Top right: GFP (green) is localized in the cytoplasm, and ProteoStat aggresome dye (red) stains the intracellular PSPAs of Mut1 neurons. Bottom right: magnified view of the aggregate depicted in the white square above.

(D) Schematic of rescue with NGLY1 lentivirus in Mut over the time course of *in vitro* differentiation.

(E) Representative images following staining with ProteoStat aggresome dye (red) on neurons derived from the iPSCs of NGLY1-deficient patients, isogenic control neurons, and NGLY1-deficient patients that have been transduced with lentivirus. Neurons were stained

Author Manuscript Author Manuscript Author Manuscript Author Manuscript

Author Manuscript Author Manuscript Author Manuscript Author Manuscript

4 weeks after differentiation. GFP (green; NGN2 transduced neuron); DAPI (blue; nuclear stain). Scale bar, 10 μm.

(F) The percentage of neurons positive for the aggresome dye was quantified by counting approximately 120 patient-derived (Mut) and NGLY1 lentivirus-transduced patient-derived (Mut+NGLY1) neurons. Individual values are presented as a mean ± SEM. **$p < 0.005$, ***$p < 0.0005$, Mann-Whitney U test.

Author Manuscript Author Manuscript Author Manuscript Author Manuscript

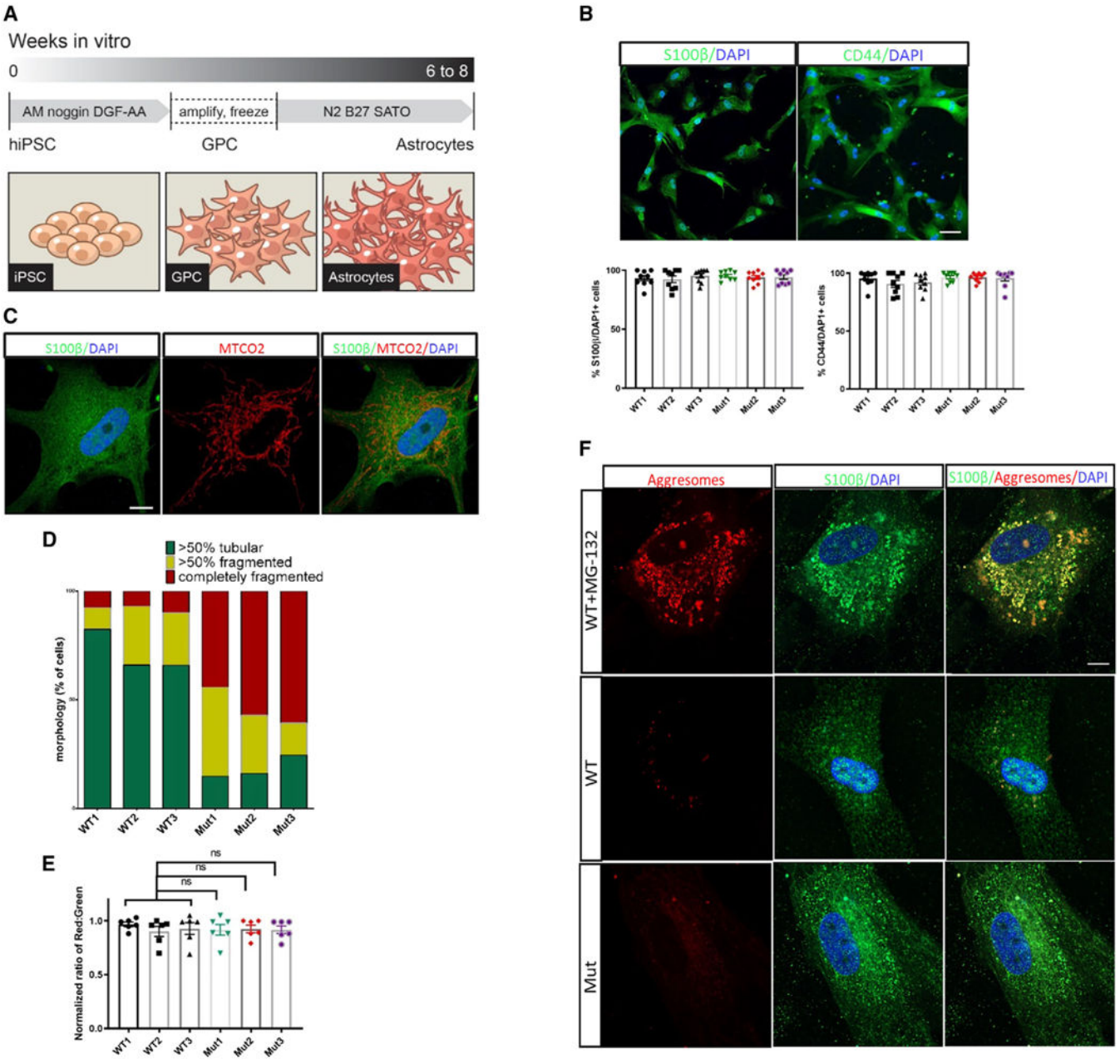

Figure 4. Differentiation of NGLY1 astrocytes via glial progenitor cells

(A) Schematic representation of the experimental paradigm used for differentiation of human astrocytes over a total time of 6–8 weeks. Human iPSCs were used to generate floating embryoid bodies, followed by dissociated glial progenitor cells (GPCs), and were differentiated to astrocytes in monolayers.

(B) Representative fluorescent images of immunostainings for control and NGLY1-deficient patient astrocytes (4-week differentiation post-GPCs; 6-week differentiation for GFAP) expressing S100β (green) and CD44 (green). All cells were counterstained for DAPI (blue). Scale bars, 20 μm. Quantifications for percentage of astrocytes; positive for the listed

Author Manuscript Author Manuscript Author Manuscript Author Manuscript

markers over DAPI. Results are expressed as means ± SEM, n = 3 experiments for iPSC-derived lines.

(C) Representative immunofluorescence images of MTCO2 (mitochondrial marker), with the proportion of mitochondria in each category is shown in (D), for WT and NGLY1 mutant astrocytes at 6 weeks post-differentiation. Scale bar, 10 μm.

(E) Quantification of MMP in NGLY1 astrocytes compared with controls. Individual measurements were performed in duplicate from 3 different experiments. Individual values are presented as a mean ± SEM. Not significant (ns) = $p > 0.05$, one-way ANOVA with Dunnett's post hoc test.

(F) Representative images following staining with ProteoStat aggresome dye (red) on astrocytes derived from the iPSCs of NGLY1-deficient patients and isogenic control neurons. Astrocytes were stained 6 weeks after differentiation. S100β (green); DAPI (blue; nuclear stain). Treatment with the proteasome inhibitor MG-132 serves a positive control demonstrating the induction of PSPA formation in control cells. Scale bar, 10 μm.

Author Manuscript
Author Manuscript
Author Manuscript
Author Manuscript

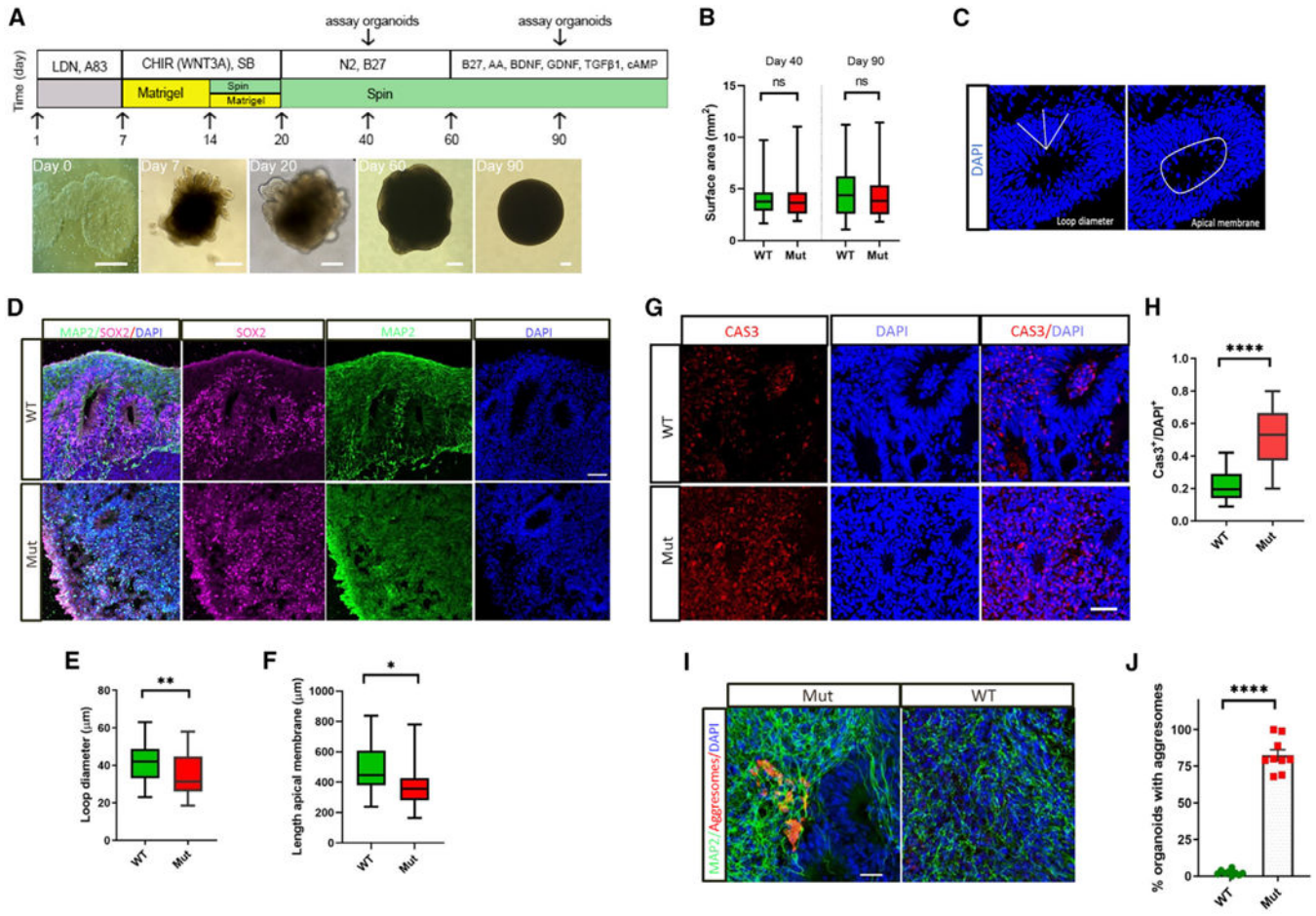

Figure 5. Phenotypes of NGLY1 organoids

(A) Schematic diagram of forebrain organoid protocol and sample phase images at different stages. Scale bars, 200 μm.

(B) Size of control (WT1, WT2) and NGLY1-deficient (Mut1 and Mut2) patient-derived forebrain-type organoids at two time points. n = 30 organoids for each clone. Data are presented as boxplots illustrating 80% of the data distribution. 10^{th}, 25^{th}, median, 75^{th}, and 90^{th} percentiles are shown for these and all subsequent boxplots. ns = $p > 0.05$, Mann-Whitney U test.

(C) Schematic illustration of how loop diameter and length of apical membrane were quantified.

(D) Representative images of immunocytochemical characterization of organoids at day 40 ± 5. Organoids organize in multiple neuroepithelial loops. Organoids are stained with neural progenitor marker SOX2 (pink), neuronal marker MAP2 (green), and DAPI (blue). Scale bar, 50 μm.

(E and F) Quantification of the (E) loop diameter and (F) length of apical membrane in controls (n = 58) and patients (n = 57). Results are expressed as means ± SEM, n = 3 experiments. *$p < 0.05$, **$p < 0.005$, Mann-Whitney U test.

(G) Representative images of immunocytochemical staining of organoids at day 40 ± 5. Organoids are stained with caspase-3, CAS3 (red), and DAPI (blue). Scale bar, 40 μm.

Author Manuscript Author Manuscript Author Manuscript Author Manuscript

(H) Quantification of the caspase-3-positive cells in the ventricular zone (VZ)-like and subventricular zone (SVZ)-like regions in day-40 organoid sections (of WT1, WT2, Mut1, and Mut2). Results are expressed as means ± SEM, n = 3 experiments. ****p < 0.00005, Mann-Whitney U test.

(I) Representative images following use of ProteoStat aggresome dye (red) on organoids at 100 days of differentiation *in vitro*. MAP2, neuronal marker (green); DAPI, nuclei marker (blue). Scale bar, 20 μm.

(J) The percentage of organoids positive for the aggresome dye was quantified by counting approximately 100 organoids. Individual values are presented as a mean ± SEM. ****p < 0.00005, Mann-Whitney U test.

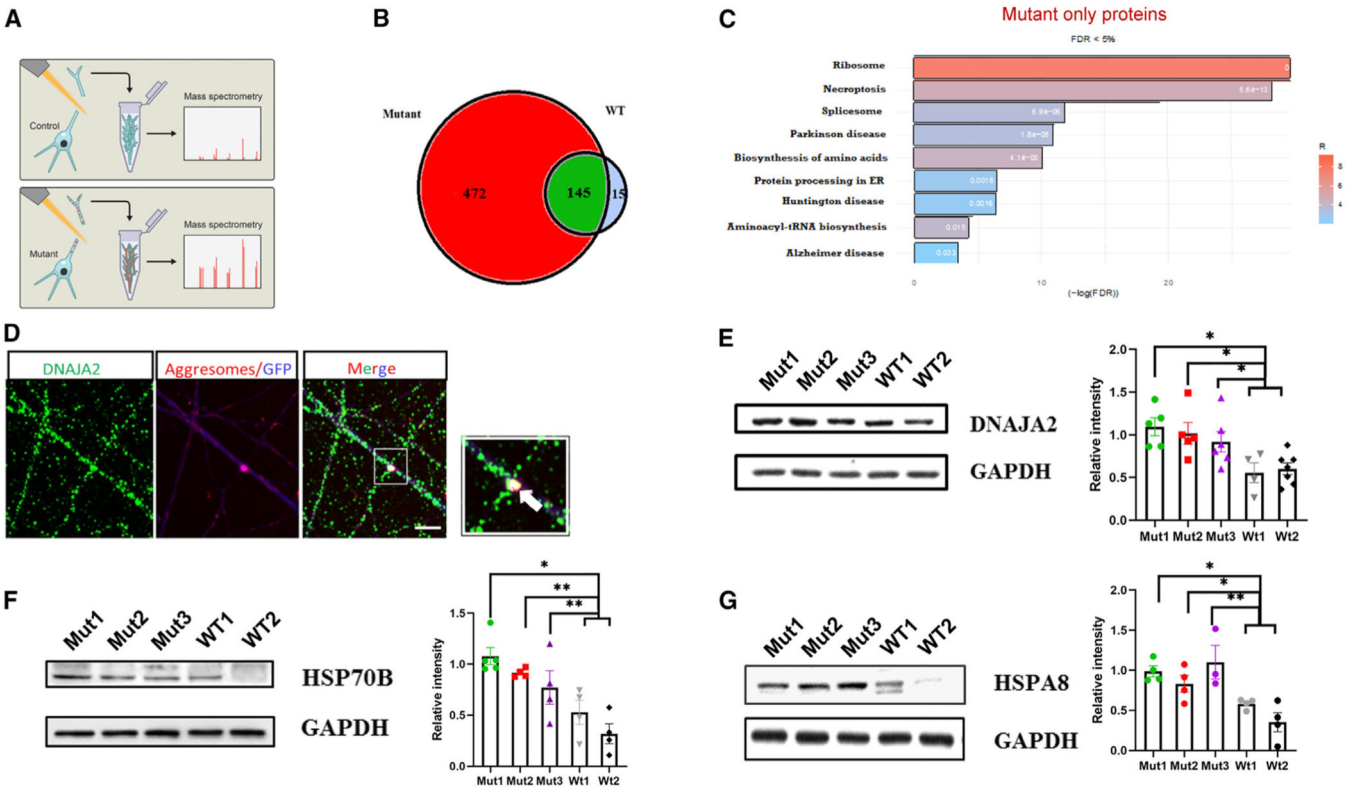

Figure 6. Functional characterization of NGLY1 PSPAs

(A) Schematic of laser capture microscopy rationale.

(B) Venn diagram of unique and shared proteins in NGLY1 neurons identified by mass spectroscopy. Results are from 2 experiments, n = 7 for each group.

(C) Protein ontology over-representation analysis of NGLY1 neurites, performed using WebGestaltR v.0.3.1 and the KEGG pathway database. Terms were considered over-represented using a false discovery threshold of 0.05.

(D) Representative images following use of DNAJA2 (green) and ProteoStat aggresome dye (red) on neurites at 4 weeks of neural differentiation. GFP (blue). Scale bar, 5 μm. Arrow indicates co-localization of the DNAJA2 and ProteoStat aggresome dye.

(E–G) Immunoblotting with anti-HSPA8 (G), HSP70B (F), and DNAJA2 (E) antibodies (70, 70, and 50 kDa, respectively); loading control (bottom, 37 kDa). Right: quantification for each stain. Specific immunoreactive signals for DNAJA2 subunits from iPSC-derived neurons in each lane (integral band intensity) were normalized to the corresponding GAPDH band intensity. Results are expressed as means ± SEM, n = 3 or 4 experiments. *p < 0.05, **p < 0.005, one-way ANOVA with Dunnett's post hoc test.

Author Manuscript Author Manuscript Author Manuscript Author Manuscript

Author Manuscript Author Manuscript Author Manuscript Author Manuscript

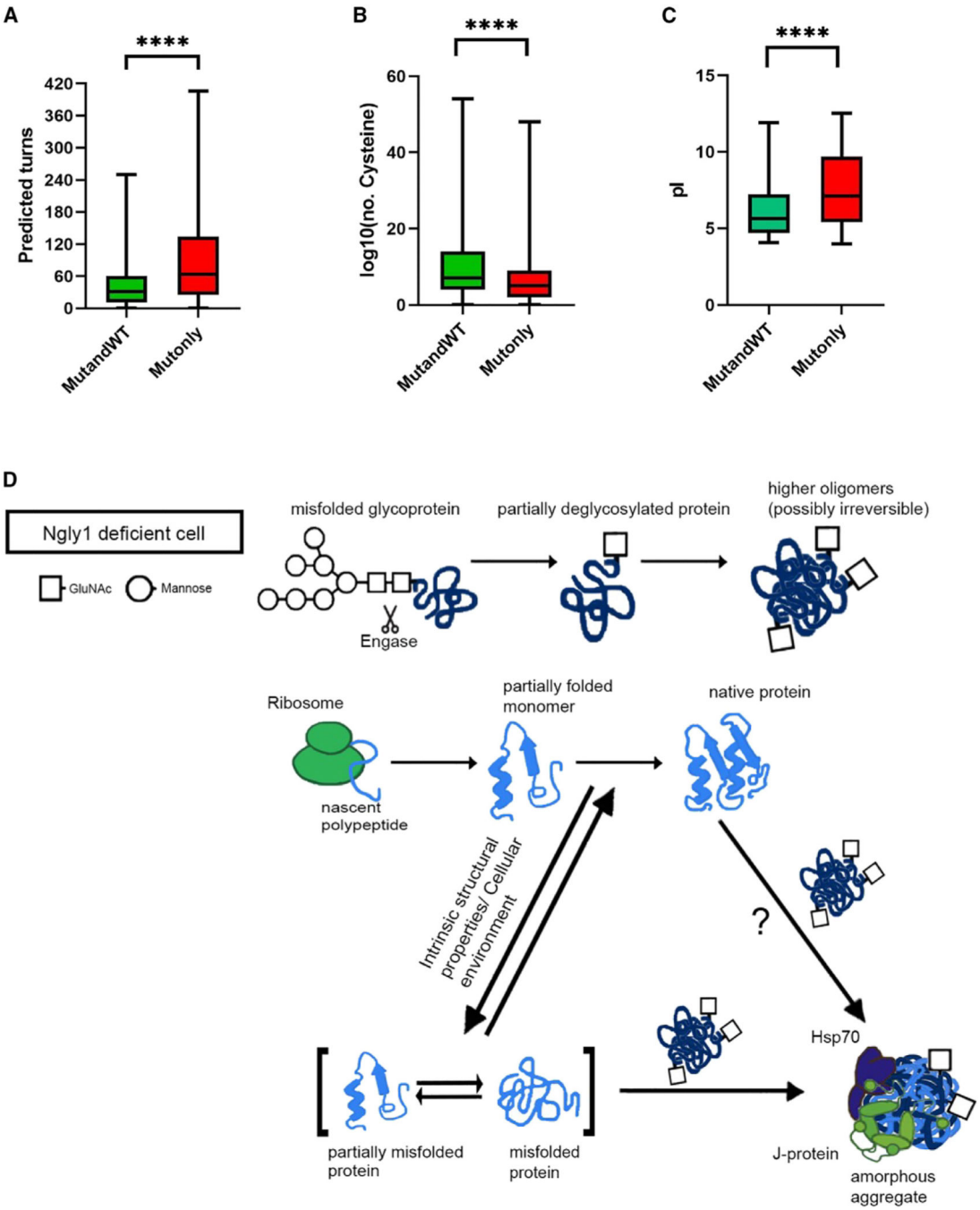

Figure 7. Structural characterizations of NGLY1 PSPAs

(A–C) Structural characterizations of proteins that are uniquely found in mutant neurites or are common between mutant and control neurites. ns = $p > 0.05$, ****$p < 0.00005$, Mann-Whitney U test.

(D) Proposed mechanism of aggresome formation in NGLY1-deficient neurons. In NGLY1-deficient cells, endo-beta-N-acetylglucosaminadase (ENGase) acts stochastically to cleave glycans on misfolded glycoproteins. Reaction of ENGase with misfolded glycoproteins results in the formation of N-GlcNAc proteins that may in turn cause the formation of

Author Manuscript Author Manuscript Author Manuscript Author Manuscript

toxic protein aggregates. After synthesis from the ribosome, a protein folds through different intermediates to its native structure. Several factors can cause protein misfolding. Once present, misfolded intermediates can be refolded to the native state or be degraded by different cellular proteolysis systems that prevent the accumulation of misfolded proteins. If the quality-control network is overwhelmed, for example with N-GlcNAc proteins and/or through persisting stress conditions, increased amounts of aberrant proteins can form. Their further aggregation can be influenced by the presence of N-GlcNAc proteins. Forming aggregates will mostly be an apparently unordered aggregation of proteins, with each individual protein not generally associated with disease. Molecular chaperones will be a significant presence in these aggregates to provide folding assistance.

Author Manuscript Author Manuscript Author Manuscript Author Manuscript

KEY RESOURCES TABLE

REAGENT or RESOURCE	SOURCE	IDENTIFIER
Antibodies		
Rabbit anti-TBR2 (1:200)	abcam	ab23345
Rabbit anti-Tuj1 (1:200)	Covance	PRB-435P
Rabbit anti-PAX6 (1:200)	Biolegend	901301
Chicken anti-MAP2 (1:300)	abcam	ab5392
Rabbit anti-NeuN (1:300)	Invitrogen	PA5-56560
Rat anti-CTIP2 (1:200)	abcam	ab18465
Rat anti-SOX2 (1:200)	Invitrogen	14-9811-82
Rabbit anti-SATB2(1:200)	abcam	ab6999
Rabbit anti-a-Syn (1:200)	Cell Signaling	2628S
Mouse anti-B-amyloid (1:200)	Covance	SIG-39220
Rabbit anti-Cas3 (1:200)	Cell Signaling	9664
Mouse anti-Ki67 (1:200)	Milipore	MAB4190
Rabbit anti-FOXG1 (1:200)	abcam	ab18259
Mouse anti-DNAJA2 (1:200)	Origene	TA501710
Mouse anti-HSPA8 (1:200)	RnD Systems	MAB4148
Rabbit anti-RPLP0 (1:1000)	Novus	NBP1-57528
Rabbit anti-HSPA2 (1:1000)	Novus	NBP1-58213
Rabbit anti-SQSTM1 (1:1000)	Invitrogen	PA5-20839
Rabbit anti-UCHL1 (1:1000)	CST	3524S
Mouse anti-HSP70B (1:1000)	ENZO	ADI-SPA-754
Rabbit anti-TCF11/NRF1 (1:1000)	CST	8052S
Rabbit anti-HSP90 (1:1000)	Biovision	3389-30t
Rabbit anti-HSP40 (1:1000)	Novus	NBP2-38988
Mouse anti-GAPDH (1:10000)	Fitzgerald	10R-G109A
Succinylated WGA (1:2500)	Vector Laboratories	B-1025S
Concanavalin A (1:4000)	Vector Laboratories	B-1005
Streptavidin HRP	CST	3999S
Biological samples		
Mut1	Courtesy of Dr. Guangwen Wang, Stanford University	CP1
WT1	Courtesy of Dr. Guangwen Wang, Stanford University	CP1-E8C
WT2	Courtesy of Dr. Guangwen Wang, Stanford University	CP1-E11C
WT3	Courtesy of Dr. Guangwen Wang, Stanford University	CP1-E8-11C
Mut2	Courtesy of Dr. Guangwen Wang, Stanford University	CP2
Mut3	Courtesy of Dr. Guangwen Wang, Stanford University	CP7
Critical commercial assays		
PROTEOSTAT AGGRESOME DETECTION KIT	Enzo	ENZ-51035-K100
Deposited data		
Raw RNA-seq data	This Study	GEO: GSE197454
Raw Proteomics data	This Study	PXD031091